Astronomy & Astrophysics manuscript no. Carney_2015_EmbYSOs
November 11, 2015
©ESO 2015

Classifying the embedded young stellar population in Perseus and Taurus & the LOMASS database

M.T. Carney[1], U.A. Yıldız[1,2], J.C. Mottram[1], E.F. van Dishoeck[1,3], J. Ramchandani[1], J.K. Jørgensen[4,5]

[1] Leiden Observatory, Leiden University, PO Box 9513, 2300 RA, The Netherlands.
e-mail: masoncarney@strw.leidenuniv.nl
[2] Jet Propulsion Laboratory, California Institute of Technology, 4800 Oak Grove Drive, Pasadena CA, 91109, USA
[3] Max-Planck Institut fur Extraterrestriche Physik, Giessenbachstrasse 1, 85748 Garching, Germany
[4] Niels Bohr Institute, University of Copenhagen, Juliane Maries Vej 30, DK-2100 Copenhagen Ø., Denmark
[5] Centre for Star and Planet Formation, Natural History Museum of Denmark, University of Copenhagen, Øster Voldgade 5-7, DK-1350 Copenhagen K., Denmark

Received 14 April 2015 / Accepted 11 September 2015

arXiv:1511.03136v1 [astro-ph.SR] 10 Nov 2015

ABSTRACT

Context. The classification of young stellar objects (YSOs) is typically done using the infrared spectral slope or bolometric temperature, but either can result in contamination of samples. More accurate methods to determine the evolutionary stage of YSOs will improve the reliability of statistics for the embedded YSO population and provide more robust stage lifetimes.
Aims. We aim to separate the truly embedded YSOs from more evolved sources.
Methods. Maps of HCO^+ J=4–3 and $C^{18}O$ J=3–2 were observed with HARP on the James Clerk Maxwell Telescope (JCMT) for a sample of 56 candidate YSOs in Perseus and Taurus in order to characterize the presence and morphology of emission from high density (n_{crit} >10^6 cm^{-3}) and high column density gas, respectively. These are supplemented with archival dust continuum maps observed with SCUBA on the JCMT and *Herschel* PACS to compare the morphology of the gas and dust in the protostellar envelopes. The spatial concentration of HCO^+ J=4–3 and 850 μm dust emission are used to classify the embedded nature of YSOs.
Results. Approximately 30% of Class 0+I sources in Perseus and Taurus are not Stage I, but are likely to be more evolved Stage II pre-main sequence (PMS) stars with disks. An additional 16% are confused sources with an uncertain evolutionary stage. Outflows are found to make a negligible contribution to the integrated HCO^+ intensity for the majority of sources in this study.
Conclusions. Separating classifications by cloud reveals that a high percentage of the Class 0+I sources in the Perseus star forming region are truly embedded Stage I sources (71%), while the Taurus cloud hosts a majority of evolved PMS stars with disks (68%). The concentration factor method is useful to correct misidentified embedded YSOs, yielding higher accuracy for YSO population statistics and Stage timescales. Current estimates (0.54 Myr) may overpredict the Stage I lifetime on the order of 30%, resulting in timescales of 0.38 Myr for the embedded phase.

1. Introduction

Low-mass young stellar objects (YSOs) have traditionally been classified based on their observed infrared slope (α_{IR}) in the wavelength range from 2 to 20 μm (Lada & Wilking 1984) or their bolometric temperature (T_{bol}, Myers & Ladd 1993). In the earliest phases of star formation, most of the emission appears at far-IR and submillimeter wavelengths. Such observationally based evolutionary schemes start with Class 0 (Andre et al. 2000), the earliest phase of low-mass star formation, where the protostar is still deeply embedded. This phase only lasts a short time, ~0.15 Myr according to Evans et al. (2009). Class 0 is followed by Class I, with a combined Class 0+I halflife of ~0.5 Myr representing the embedded phase of the protostar, then Class II, and Class III as the spectral energy distribution (SED) of the source shifts towards optical wavelengths and gradually loses intensity at far-IR/sub-mm wavelengths. The term "Class" refers only to an observational phase defined by α_{IR} and/or T_{bol}, whereas "Stage" refers to a phase of low-mass star formation based on physical parameters.

Physical definitions of YSOs use parameters such as star, disk, and envelope mass ratios to determine the evolutionary stage (Adams et al. 1987; Whitney et al. 2003b,a; Robitaille et al. 2006). In Stage I, the protostar is surrounded by a collapsing envelope and a circumstellar disk through which material is accreted onto the growing star ($M_{env} > M_{star}$ at very early times). This stage is critical for the subsequent evolution since the mass of the star and the physical and chemical structure of the circumstellar disk are determined here. These protostars also power bipolar outflows with a very high degree of collimation, and there is evidence of shock processing of molecular gas even in cases of very low stellar luminosity (Tafalla et al. 2000; Dunham et al. 2008). As the YSO evolves the envelope is dispersed by the outflow, the disk grows, the object becomes brighter at IR wavelengths, and the outflows diminish in force. Stage I embedded sources ($M_{disk}/M_{envelope} < 2$ and $[M_{disk} + M_{envelope}] < M_{star}$) differ from Stage II gas-rich classical T Tauri stars ($M_{envelope} \lesssim 0.2 M_\odot$ and $M_{disk}/M_{star} \ll 1$), which are more evolved pre-main sequence (PMS) objects and often have an associated circumstellar disk. Stage I sources may also be distinguished from Stage II sources through enhanced continuum veiling of the young central star, as seen in their near-infrared spectra (e.g., Casali & Matthews 1992; Greene & Lada 1996; White & Hillenbrand 2004).

Lifetimes of astronomical objects are generally inferred by counting the number of objects in each phase and taking the age of one of these phases to be known (e.g., Evans et al. 2009; Mottram et al. 2011). In star formation, the reference for low-mass

protostars is usually the lifetime of the Class II T Tauri phase, generally corresponding to Stage II physical parameters, which is ∼2–3 Myr based on current estimates (Haisch et al. 2001; Spezzi et al. 2008; Muench et al. 2007; Evans et al. 2009). However, this method assumes that the classification methods for all phases are correct and complete. Previous studies have shown that the above-mentioned criteria based on α_{IR} or T_{bol} lead to samples with significant contamination: some Class 0+I sources turn out to be edge-on Stage II PMS stars with disks, or sources obscured by cloud material due to projection effects (Brandner et al. 2000; Lahuis et al. 2006). Models indicate that such confusion may be quite common and can include up to 30% of the total embedded sources (Whitney et al. 2003b; Robitaille et al. 2006; Crapsi et al. 2008). Comparison between single-dish and interferometric (sub-)mm observations is able to correctly identify such sources (Lommen et al. 2008; Crapsi et al. 2008). However, the capabilities of current interferometers make this method quite time consuming, and it is limited to only a small number of the brightest sub-mm sources.

Using the 345 GHz Heterodyne Array Receiver Program (HARP, Buckle et al. 2009) and Submillimeter Common-User Bolometer Array (SCUBA, Holland et al. 1999) instruments on the James Clerk Maxwell Telescope [1] (JCMT), van Kempen et al. (2009) identified truly embedded sources without the need for interferometry, by instead comparing maps of HCO^+ J=4–3, $C^{18}O$ J=3–2, and 850 μm dust emission over an approximately 2′ region around each source at a spatial resolution of ∼15″. In these maps, HCO^+ 4–3 ($n_{crit} > 10^6$ cm^{-3}) emission traces the presence of dense gas in the envelope , and $C^{18}O$ 3–2 ($n_{crit} > 10^4$ cm^{-3}) traces the column density. HCO^+ 4–3 can also be an effective tracer of outflows in early phase YSOs and over large spatial regions (Walker-Smith et al. 2014). Both the absolute line strengths and their variation over the region (concentration) play a crucial role in the identification of embedded sources. van Kempen et al. (2009) applied this method to all sources in Ophiuchus that were thought to be Class I based on the traditional criteria, and they found that all tracers are centrally concentrated for truly embedded sources, with the possible exception of $C^{18}O$. Some sources appear unresolved, but are still bright in both HCO^+ 4–3 and $C^{18}O$ 3–2 (>1 K km s^{-1}). In contrast, edge-on disks or obscured sources have weak point-like and/or flat sub-mm dust emission, respectively, when observed with SCUBA. In molecular emission they have a flat $C^{18}O$ 3–2 emission distribution (if any) and/or a HCO^+ 4–3 intensity of at most 0.3 K km s^{-1}. By using this method, 16 out of 38 Class I and flat SED (intermediate between Class I and II) sources were found to be truly embedded Stage I YSOs in Ophiuchus, whereas the remainder were characterized as Stage II evolved PMS stars with disks and/or obscured sources (van Kempen et al. 2009). An earlier single pointing HCO^+ 3–2 study by Hogerheijde et al. (1997) of a number of Taurus Class I sources also found a significant fraction of them to be Stage II objects.

These new statistics clearly affect the lifetime of the embedded phase, implying that the Stage I lifetime has been overestimated, at least for Ophiuchus. This paper aims to apply these same criteria to sources in the Perseus and Taurus star-forming regions. In addition, the robustness of using just a single HCO^+ spectrum at the source position versus complete maps to classify sources is investigated: only central source spectra are available for the bulk of the many hundreds of Class 0+I and flat-spectrum sources found in nearby star-forming regions (Heiderman & Evans 2015).

The structure of the paper is as follows: Section 2 outlines the telescopes and instruments used during observations and the data collected from previous surveys. Section 3 provides details on the properties of central spectra extracted from the observations and categorizes the morphology of the spatial data at each wavelength. Section 4 describes the method to classify the objects in the sample as truly embedded YSOs versus more evolved sources. Section 5 describes the LOMASS database. Section 6 provides the conclusions.

2. Observations

An overview of the source list is given in Table 1. Sources and their coordinates are taken from the following: Perseus Class 0+I sources from Jørgensen et al. (2007), Taurus targets from the Class 0+I sample in Hartmann (2002) with additional sources derived from a comparison between SCUBA and *Spitzer* data in the region (Jørgensen, priv. comm.), and Serpens sources selected from Enoch et al. (2007). The sources were chosen to include known Class 0+I ($\alpha_{IR} \geq 0.3$) objects in these clouds at the time of selection (2008), with some borderline flat spectrum sources ($0.3 > \alpha_{IR} \geq -0.3$) included. Table 1 includes alternate, more common names for many of the objects, which are sometimes included parenthetically in the text.

Infrared slope values (α_{IR}) obtained from the c2d catalogue are presented in Column 7 of Table 1 for all overlapping sources observed in the c2d survey. These values may differ from α_{IR} at the time of selection. Extinction-corrected slopes obtained from Dunham et al. (subm.) are also shown. There is only one source for which there is a change in Class assignment: J032738.2+301358 (L1455-FIR 2) moves from a Flat spectrum to a Class II source. All other sources are unaffected.

Spatially resolved maps are obtained for 56 sources in the Perseus (d = 250pc) and Taurus (d = 140pc) star forming molecular clouds in both HCO^+ 4–3 at 356.734 GHz and $C^{18}O$ 3–2 at 329.330 GHz with the JCMT HARP instrument (Buckle et al. 2009) using the ACSIS backend (Dent et al. 2000) in jiggle position-switch mode. An additional nine sources in the Serpens (d = 260pc) cloud were mapped in $C^{18}O$ 3–2 only. HARP is a heterodyne array with 16 SIS detectors in a 4 x 4 configuration with pixel separations of 30″. Array pixels have typical single side-band system temperatures of 300−350 K. The total foot print of the receiver is 2′×2′ with a diffraction limited beam of ∼15″. The offset switch used a slew of 1 degree in RA for sky background measurements.

The HARP observations were carried out between 2008 and 2011 in good atmospheric conditions (optical depth $\tau_{225GHz} \leq 0.1$). Typical rms noise levels are 0.15 K after resampling the spectra into 0.2 km s^{-1} bins. To achieve these noise levels, typical integration times were ∼30 minutes on- and off-source to scan the whole 2′×2′ region for both lines. All HARP data were converted to main beam brightness temperature $T_{mb} = T_A^*/\eta_{mb}$, where the beam efficiency of HARP is set to $\eta_{mb} = 0.63$. Calibration errors are estimated to be ∼20% (Buckle et al. 2009). All HARP data were reduced using the GILDAS-CLASS[2] software package.

In order to compare spectral observations to the dust continuum, data were taken from archival surveys of the JCMT

[1] The James Clerk Maxwell Telescope has historically been operated by the Joint Astronomy Centre on behalf of the Science and Technology Facilities Council of the United Kingdom, the National Research Council of Canada and the Netherlands Organisation for Scientific Research.

[2] http://www.iram.fr/IRAMFR/GILDAS

Table 1: Source coordinates, infrared slope values, and central spectra properties.

Object Name	Alternate Name(s)[a]	Cloud	RA [J2000]	DEC [J2000]	Class[b]	α_{IR}[c]	V_{lsr}[d]	HCO$^+$ 4–3			C^{18}O 3–2		
			[hh:mm:ss]	[dd:mm:ss]			[km s^{-1}]	$\int T_{mb} dV$ [K km s^{-1}]	T_{mb} [K]	FWHM [km s^{-1}]	$\int T_{mb} dV$ [K km s^{-1}]	T_{mb} [K]	FWHM [km s^{-1}]
J032522.3+304513	L1448-IRS 2, Pers01	Perseus	03:25:22.4	30:45:13.6	I (I)	2.3 (2.2)	4.1	2.9±0.09	1.9	1.5	2.4±0.06	2.8	0.7
J032536.4+304523	L1448-N, Pers02	Perseus	03:25:36.5	30:45:23.2	I (I)	2.6 (2.6)	4.6	14.8±0.1	6.2	2.2	6.7±0.2	4.0	1.4
J032637.4+301528	Pers-4, Pers04	Perseus	03:26:37.5	30:15:28.2	I (I)	1.1 (1.0)	5.2	1.1±0.04	1.1	0.5	0.8±0.08	1.1	0.8
J032738.2+301358	L1455-FIR 2	Perseus	03:27:38.3	30:13:58.5	F (II)	-0.2 (-0.4)	4.4	1.7±0.06	1.0	1.7	0.8±0.09	0.7	1.0
J032743.2+301228	L1455-IRS 4	Perseus	03:27:43.3	30:12:28.9	I (I)	2.4 (2.2)	5.0	2.2±0.06	2.0	0.9	1.2±0.1	1.3	1.2
J032832.5+311104	Pers-9	Perseus	03:28:32.6	31:11:04.8	I (I)	0.8 (0.5)	7.5	2.5±0.1	1.4	1.9	E/A	E/A	E/A
J032834.5+310705	Pers-10	Perseus	03:28:34.5	31:07:05.5	I (I)	0.5 (0.3)	–	E/A	E/A	E/A	A	A	A
J032837.1+311328	IRAS03255+3103, Pers05	Perseus	03:28:37.1	31:13:28.3	–	–	7.3	4.0±0.08	4.0	1.2	2.1±0.08	3.0	0.7
J032839.1+310601	Pers-12	Perseus	03:28:39.1	31:06:01.6	I (I)	1.7 (1.6)	7.2	0.6±0.05	1.2	0.5	0.5±0.07	0.8	0.4
J032840.6+311756	Pers-13	Perseus	03:28:40.6	31:17:56.5	I (I)	1.0 (1.0)	8.1	1.3±0.1	1.4	1.0	1.0±0.06	1.6	0.8
J032845.3+310541	IRAS03256+3055	Perseus	03:28:45.3	31:05:41.9	I (I)	1.1 (1.1)	7.4	1.0±0.04	1.4	0.7	E/A	E/A	E/A
J032859.5+312146	Pers-17	Perseus	03:28:59.3	31:21:46.7	II (II)	-0.8 (-1.1)	7.7	6.4±0.06	4.0	1.5	7.2±0.1	4.5	1.6
J032900.6+311200	Pers-18, Pers07	Perseus	03:29:00.6	31:12:00.4	I (I)	2.2 (2.0)	7.4	2.6±0.06	2.4	1.0	1.5±0.1	1.1	1.3
J032901.6+312028	Pers-19, Pers08	Perseus	03:29:01.7	31:20:28.5	–	–	7.9	12.1±0.06	8.0	1.5	9.2±0.1	6.0	1.3
J032903.3+311555	SVS13	Perseus	03:29:03.3	31:15:55.5	–	–	8.2	12.4±0.08	7.0	1.6	8.3±0.1	4.7	1.5
J032904.0+311446	HH 7-11 MMS6	Perseus	03:29:04.1	31:14:46.6	I (I)	1.4 (1.3)	9.0	8.3±0.08	4.4	1.9	4.7±0.1	2.5	1.9
J032910.7+311820	Pers-23, Pers10	Perseus	03:29:10.7	31:18:20.5	I (I)	2.0 (1.9)	8.6	5.7±0.1	3.7	1.4	4.8±0.09	3.2	1.3
J032917.2+312746	Pers-27	Perseus	03:29:17.2	31:27:46.2	I (I)	1.8 (1.7)	7.6	2.6±0.06	2.7	0.9	2.7±0.07	3.3	0.7
J032918.2+312319	Pers-28	Perseus	03:29:18.3	31:23:19.9	I (I)	1.3 (1.1)	7.7	1.2±0.07	2.1	0.6	3.6±0.08	4.2	0.9
J032923.5+313329	IRAS03262+3123	Perseus	03:29:23.5	31:33:29.4	I (I)	1.5 (1.5)	7.5	1.0±0.05	1.7	0.6	0.9±0.08	1.9	0.4
J032951.8+313905	IRAS03267+3128, Pers13	Perseus	03:29:51.9	31:39:05.6	I (I)	3.4 (3.4)	8.0	3.5±0.05	3.5	1.0	1.8±0.1	2.0	0.7
J033121.0+304530	IRAS03282+3035, Pers15	Perseus	03:31:21.0	30:45:30.0	I (I)	1.0 (1.5)	7.0	3.3±0.07	2.8	1.3	1.0±0.2	1.0	1.4
J033218.0+304946	IRAS03292+3039, Pers16	Perseus	03:32:18.0	30:49:46.9	I (I)	1.1 (0.9)	7.0	3.9±0.07	3.8	1.2	2.8±0.2	2.0	1.0
J033313.8+312005	Pers-34	Perseus	03:33:13.8	31:20:05.2	I (I)	1.4 (1.3)	7.0	0.5±0.05	0.7	0.7	E/A	E/A	E/A
J033314.4+310710	B1-SMM3, Pers17	Perseus	03:33:14.4	31:07:10.8	I (I)	2.2 (2.7)	6.6	1.9±0.06	1.9	0.8	2.9±0.1	2.1	1.2
J033320.3+310721	B1-b	Perseus	03:33:20.3	31:07:21.4	I (I)	0.9 (0.6)	6.6	2.7±0.1	1.9	1.3	2.9±0.1	2.4	1.2
J033327.3+310710	Pers-40, Pers19	Perseus	03:33:27.3	31:07:10.2	I (I)	1.9 (1.8)	6.9	1.5±0.06	1.5	0.9	2.3±0.2	2.8	0.8
J034350.9+320324	Pers-41	Perseus	03:43:50.9	32:03:24.7	I (I)	1.5 (1.4)	8.6	2.9±0.1	2.8	1.0	3.1±0.1	2.7	0.9
J034356.9+320304	IC 348-MMS, Pers21	Perseus	03:43:56.9	32:03:04.2	I (I)	1.4 (1.8)	8.8	4.7±0.07	3.8	1.1	4.3±0.1	4.8	0.8
J034357.3+320047	HH 211-FIR	Perseus	03:43:57.3	32:00:47.6	F (F)	0.02 (-0.07)	9.0	7.0±0.1	3.2	2.1	3.7±0.1	4.5	0.8
J034359.4+320035	Pers-46	Perseus	03:43:59.4	32:00:35.5	F (F)	0.1 (-0.2)	8.6	1.5±0.09	0.5	1.7	1.9±0.2	1.8	1.1
J034402.4+320204	Pers-47	Perseus	03:44:02.4	32:02:04.7	I (I)	1.5 (1.5)	8.9	4.2±0.06	4.0	1.0	5.3±0.2	4.3	1.1
J034443.3+320131	IRAS03415+3152, Pers22	Perseus	03:44:43.3	32:01:31.6	I (I)	0.5 (0.6)	9.8	5.2±0.1	2.5	2.1	4.9±0.2	3.7	1.2
J034741.6+325143	B5-IRS 1	Perseus	03:47:41.6	32:51:43.9	I (I)	0.8 (1.3)	10.1	1.7±0.07	1.8	0.6	1.7±0.1	2.0	0.8
J041354.7+281132	L1495-IRS	Taurus	04:13:54.7	28:11:32.9	I[K]	–	6.8	<0.38	–	–	0.9±0.2	0.9	1.0
J041412.3+280837	IRAS04111+2800	Taurus	04:14:12.3	28:08:37.3	–	–	7.1	<0.35	–	–	0.9±0.2	0.9	0.9
J041534.5+291347	IRAS04123+2906	Taurus	04:15:34.5	29:13:47.0	–	–	–	<0.40	–	–	<0.43	–	–
J041851.4+282026	CoKu Tau 1	Taurus	04:18:51.5	28:20:26.5	II[K]	–	7.3	<0.34	–	–	0.8±0.1	1.4	0.6
J041942.5+271336	IRAS04166+2706	Taurus	04:19:42.5	27:13:36.4	I[K]	–	6.7	3.3±0.2†	2.5	1.4	0.8±0.2	1.3	0.5
J041959.2+270958	IRAS04169+2702, Tau01	Taurus	04:19:59.2	27:09:58.6	I[K]	–	6.8	1.8±0.1	2.0	0.9	2.1±0.1	2.2	0.8
J042110.0+270142	IRAS04181+2655	Taurus	04:21:10.0	27:01:42.0	I[K]	–	6.9	0.5±0.1	1.3	0.5	1.2±0.09	1.3	0.6
J042111.4+270108	IRAS04181+2654AB, Tau02	Taurus	04:21:11.4	27:01:08.9	I[K]	–	6.6	1.1±0.2	1.4	1.0	1.5±0.1	2.1	0.5
J042656.3+244335	IRAS04239+2436	Taurus	04:26:56.4	24:43:35.9	I[K]	–	6.7	0.6±0.2	0.5	2.4	1.7±0.1	2.3	0.8
J042757.3+261918	IRAS04248+2612, Tau06	Taurus	04:27:57.3	26:19:18.3	I[K]	–	7.3	1.9±0.1	2.1	0.8	1.0±0.1	1.1	1.1
J042838.9+265135	L1521F-IRS	Taurus	04:28:38.9	26:51:35.2	I	1.9	6.5	3.2±0.2†	2.7	1.6	0.4±0.1	1.4	0.4
J042905.0+264904	IRAS04260+2642	Taurus	04:29:05.0	26:49:04.4	I[K]	–	–	<0.45	–	–	<0.65	–	–
J042907.6+244350	IRAS04264+2433, Tau07	Taurus	04:29:07.7	24:43:50.1	I	0.4	–	<0.45	–	–	<0.41	–	–
J042923.6+243302	GV Tau	Taurus	04:29:23.7	24:33:02.0	I[K]	–	6.4	3.6±0.1	2.2	1.1	3.2±0.1	3.0	0.8
J043150.6+242418	HK Tau	Taurus	04:31:50.6	24:24:18.2	II	-0.45	–	<0.49	–	–	<0.52	–	–
J043215.4+242903	Haro 6-13	Taurus	04:32:15.4	24:29:03.4	II	-0.74	–	<0.44	–	–	<0.45	–	–
J043232.0+225726	L1536-IRS, Tau08	Taurus	04:32:32.0	22:57:26.7	I[K]	–	–	<0.68	–	–	<0.55	–	–
J043316.5+225320	IRAS04302+2247	Taurus	04:33:16.5	22:53:20.4	I[K]	–	5.5	1.6±0.2	0.4	4.6	<0.50	–	–
J043535.0+240822	IRAS04325+2402, Tau09	Taurus	04:35:35.0	24:08:22.0	I[K]	–	5.6	1.0±0.1	0.9	1.2	1.0±0.2	1.7	0.8
J043556.7+225436	Haro 6-28	Taurus	04:35:56.8	22:54:36.5	I[K]	–	–	<0.34	–	–	<0.44	–	–
J043953.9+260309	L1527	Taurus	04:39:53.9	26:03:09.7	–	–	5.8	8.2±0.2†	8.1	1.5	3.5±0.08	3.4	0.9
J044138.8+255626	XEST07-041	Taurus	04:41:38.8	25:56:26.8	F	0.1	–	<0.47	–	–	<0.43	–	–
J182844.0+005303	Ser-2	Serpens	18:28:44.0	00:53:03.0	I (I)	0.5 (0.5)	8.0	–	–	–	0.6±0.05	1.1	0.6
J182845.8+005132	Ser-3	Serpens	18:28:45.8	00:51:32.0	I (I)	1.3 (1.1)	7.9	–	–	–	0.5±0.05	0.8	0.6
J182853.0+001904	Ser-7	Serpens	18:28:53.0	00:19:04.0	I (I)	0.5 (0.3)	7.9	–	–	–	0.4±0.06	0.6	0.4
J182855.2+002928	Ser-8	Serpens	18:28:55.2	00:29:28.0	I (I)	1.9 (1.7)	8.0	–	–	–	3.0±0.08	2.8	1.1
J182855.9+004830	Ser-9	Serpens	18:28:55.9	00:48:30.0	–		8.2	–	–	–	0.5±0.06	0.9	0.4
J182900.2+003020	Ser-13	Serpens	18:29:00.2	00:30:20.0	I (I)	1.8 (1.6)	8.0	–	–	–	1.5±0.08	1.9	0.8
J182907.0+003042	Ser-14	Serpens	18:29:07.0	00:30:42.0	I (I)	1.6 (1.4)	7.8	–	–	–	4.7±0.1	3.1	1.4
J182909.6+003137	Ser-15	Serpens	18:29:09.6	00:31:37.0	I (I)	2.3 (2.1)	7.8	–	–	–	1.8±0.1	1.2	1.6
J182916.4+001815	Ser-17	Serpens	18:29:16.4	00:18:15.0	F (F)	-0.07 (0.06)	9.1	–	–	–	0.7±0.1	0.9	1.2

Notes. Upper limits are calculated at the $3\sigma_I$ level (see Section 3.1). E/A indicates an emission-absorption profile and A indicates a pure absorption profile which are omitted from further analysis due to contamination, likely by emission at the reference position.
[(a)] First alternate names for Perseus sources are from Table 3 in Jørgensen et al. (2007). Designators were taken from the Other Identifiers column or as Pers-# where the number is taken from the Number column. First alternate names for Taurus are from Hartmann (2002), SIMBAD commonly used identifiers, or the IRAS Point Source Catalogue (Beichman et al. 1988). Second alternate names for Perseus and Taurus are from the "William *Herschel* Line Legacy" (WILL) survey (Mottram et al., in prep.) overview paper. Serpens alternate names are from Table 1 of Enoch et al. (2007) as Ser-# where the number is taken from the Bolocam ID column.
[(b)] Class is assigned according to α_{IR} classification (e.g., Evans et al. 2009). Extinction-corrected Class assignment appears parenthetically. [(K)] C lass taken from SED designation in Kenyon & Hartmann (1995).
[(c)] α_{IR} taken from the *Spitzer* c2d catalogue (Evans et al. 2003). Extinction-corrected values from Dunham et al. (subm.) appear parenthetically.
[(d)] V_{lsr} values are based on Gaussian fits to the C^{18}O 3–2 line.
† Line profile of central spectrum shows asymmetry indicative of infall.

SCUBA and *Herschel*[3] PACS instruments. The SCUBA Legacy Catalogue survey (Di Francesco et al. 2008) provides data for dust emission at 450 μm and 850 μm with beam sizes of 9″ and 15″, respectively. Uncertainties in flux values are about 20% at 850 μm and up to 50% at 450 μm. *Herschel* PACS dust continuum maps at 70 μm and 160 μm were obtained from Herschel science archive observations taken as part of *Herschel* Gould

[3] *Herschel* is an ESA space observatory with science instruments provided by European-led Principal Investigator consortia and with important participation from NASA.

Belt Survey (André et al. 2010). Beam sizes for *Herschel* PACS are estimated to be about 12″ at 160 μm and 6″ at 70 μm in PACS/SPIRE parallel mode with respective uncertainties of order 20% and 10% (Poglitsch et al. 2010). Footprints of 2′×2′ were extracted from the large scale SCUBA and PACS maps to match the spatial coverage of the HARP maps. All dust maps were converted to units of Jansky beam^{-1}, where required.

Combined 2′×2′ field of view maps were assembled for JCMT HARP lines HCO$^+$ 4–3 and C^{18}O 3–2, *Herschel* PACS 70 μm and 160 μm observations, and JCMT SCUBA 450 μm and 850 μm observations. These maps allow characterization of the high density and high column density molecular line tracers and the warm and cool components of the dust continuum by observing the morphology of the emission at each wavelength. Intensity scales for all spatial maps are set to a percentage of the maximum value to create the best contrast between emission features and the background, and for easy visual comparison from source to source.

All maps can be found in Appendix C. They have been regridded to 100×100 pixel images using a linear interpolation between data points. HCO$^+$ 4–3 maps are available for 56 out of the 65 sources in our sample - these maps exist for all sources in Perseus and Taurus but those in Serpens were not observed in HCO$^+$ 4–3. All sources were observed in C^{18}O 3–2. We have a complete set of PACS maps for all sources while 21 out of 65 sources (∼30%) in the Perseus, Taurus, and Serpens sample do not have SCUBA observations. For HCO$^+$ 4–3 and C^{18}O 3–2 there are two maps in each line. The first pair are spatial maps of integrated intensity in units of K km s^{-1}, created by integrating the spectral emission with limits of integration $V_{\rm lsr} \pm 6.0 \times$ FWHM to ensure that integration is done over all emission down to the rms noise level. The second pair of maps in HCO$^+$ 4–3 and C^{18}O 3–2 display the main beam peak temperature in units of K. Peak temperature maps are expected to have roughly the same morphology as the integrated intensity maps, but the latter can potentially be contaminated by outflow wings, particularly in HCO$^+$ 4–3.

Absorption is seen in the C^{18}O 3–2 spectra of J032832.5+311104, J032834.5+310705, J032845.3+310541, and J033313.8+312005. In J032834.5+310705, there is also strong absorption in HCO$^+$ 4–3. These features drop below the continuum level, indicating that it is not self-absorption, but rather that the reference position contained emission in C^{18}O 3–2. In the case of J032834.5+310705 the switch region was also emitting in HCO$^+$ 4–3. The absorption features contaminate the data for these sources, and they are omitted from further analysis.

3. Results

3.1. Central spectra

Spectra are extracted from the central spatial pixel (spaxel) of the jiggle mode maps for sources observed in HCO$^+$ 4–3 and C^{18}O 3–2 (shown in Appendix B). Integrated intensity, main beam peak temperature, and local standard of rest velocity were extracted from the central spectra for sources with detected emission. The majority of sources can be fitted with a single Gaussian and do not exhibit a broad component of emission in either HCO$^+$ 4–3 or C^{18}O 3–2, suggesting that the bulk of the on-source integrated intensity is dominated by emission from the envelope with negligible contribution from high velocity outflows. The properties of the central spectra for all sources are presented in Table 1. Column 6 shows the local standard of rest velocity for each source based on the peak of the Gaussian fit to the C^{18}O 3–2 line. Subsequent columns give the integrated intensity and peak main beam temperature of HCO$^+$ 4–3 and C^{18}O 3–2.

Out of the 56 sources observed in both molecular lines, there are 45 detections in HCO$^+$ 4–3 and 43 detections in C^{18}O 3–2. Integrated intensities of HCO$^+$ 4–3 range from 0.5 K km s^{-1} to 14.8 K km s^{-1} while peak temperatures range from 0.4 K to 8.1 K. For C^{18}O 3–2 the integrated intensities and peak temperatures range from 0.5 K km s^{-1} to 9.2 K km s^{-1} and 0.6 K to 6.0 K, respectively. Additionally, C^{18}O 3–2 on source emission is detected for all nine sources in Serpens. On average the C^{18}O 3–2 emission in the Serpens sources is weaker than those in Perseus and Taurus. The average full width half maximum (FWHM) of the lines are 0.9 km s^{-1} and 1.3 km s^{-1} for C^{18}O 3–2 and HCO$^+$ 4–3, respectively.

Among sources that cannot be fitted easily with single Gaussians are J033314.4+310710 (B1-SMM3) and J033320.3+310721 (B1-b), which show broadening in the red component, and J032901.6+312028, which shows a broadening in the blue component (see Figures in Appendix B). The resulting integrated intensity maps of these sources may have some contribution from outflows that may cause their morphology to appear less concentrated than if only emission from the envelope were observed.

There is evident self-absorption in the HCO$^+$ 4–3 central spectra of J043953.9+260309 (L1527) in Taurus and its asymmetric, blue-dominated profile indicates infall of high density envelope material, in agreement with the inverse P Cygni line profile seen in *Herschel* water spectra by Mottram et al. (2013). Self-absorption and a blue-dominated, asymmetric infall signature in HCO$^+$ 4–3 can be seen to a lesser extent in two other sources in Taurus: J041942.5+271336 and J042838.9+265135 (L1521F-IRS). These features already provide strong evidence that these three objects in Taurus are likely Stage I YSOs. Self-absorption is detected in J032832.5+311104 and J034357.3+320047 (HH 211-FIR), but it is not accompanied by asymmetry. (See Section 4.4 for further discussion.)

Ten out of the 22 sources in Taurus lack detections in HCO$^+$ 4–3 above 3σ_I. For the integrated intensity we define $\sigma_I = \sqrt{\delta v \Delta_0 v} T_{\rm rms}$ where δv is the velocity resolution of the spectrum (0.2 km s^{-1}), $\Delta_0 v$ is the full line width down to zero intensity, and $T_{\rm rms}$ is the rms noise level at the given resolution. Here $\Delta_0 v$ is taken to be three times the sample-averaged FWHM for each of the two spectral lines observed to ensure that zero intensity limits are reached in all cases.

In the Perseus cloud, only J032834.5+310705 lacks an obvious detection due to the absorption features in its spectrum. There is an emission-absorption profile in HCO$^+$ 4–3 and pure emission in C^{18}O 3–2. These molecular line data are omitted from further analysis as the absorption prevents proper stage classification in this study. Uncontaminated data are needed to correctly characterize the source.

Of the ten HCO$^+$ 4–3 non-detections in Taurus, seven also lack a detection in C^{18}O 3–2. The absence of both of these high (column) density molecular tracers indicates that these sources are not likely to be deeply embedded YSOs. Two sources, J032845.3+310541 in Perseus and J043316.5+225320 in Taurus, are detected in HCO$^+$ 4–3 but have no detection in C^{18}O 3–2. This could be due to the absence of any high column density envelope or cloud material along the line of sight, strong freeze out of CO onto dust grains, or a relatively more isolated environment for these sources.

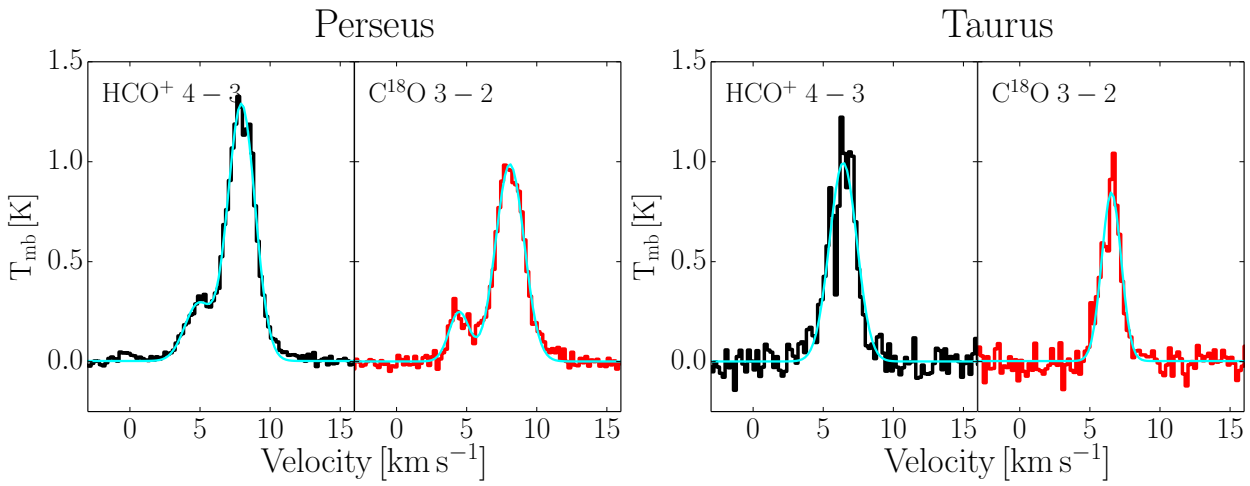

Fig. 1: Cloud-averaged spectra of all sources with detections in HCO^+ 4–3 and $C^{18}O$ 3–2. Non-detections are omitted from averaging. The HCO^+ 4–3 data are shown in black, the $C^{18}O$ 3–2 in red, and Gaussian fits in cyan. The sum of two 1D Gaussian fits is shown for the Perseus cloud. Perseus shows a clear secondary feature while Taurus is well fit by single Gaussians in both lines. Note that the y-axis scale is 0.25× the figures presented in Appendix B.

Table 2: Cloud-average central spectra properties

		HCO^+ 4–3			$C^{18}O$ 3–2		
Cloud	V_{lsr}	$\int T_{mb} dV$	T_{mb}	Δv	$\int T_{mb} dV$	T_{mb}	Δv
Perseus[a]	4.7	0.7	0.3	2.3	0.4	0.3	1.7
Perseus[b]	8.0	3.2	1.3	2.3	2.5	1.0	2.4
Taurus	6.4	2.4	1.2	2.3	1.5	1.0	1.6

Notes. Central spectra are within a 15″ beam. Local standard of rest velocity, integrated intensity, and line width are derived from the Gaussian fit. Δv is the FWHM of the Gaussian fit. Peak main beam temperature is taken as the maximum value from the data. [(a)] Fit to the weak blue component of Perseus spectra. [(b)] Fit to the strong red component of Perseus spectra.

The central spectra for each source with detections in HCO^+ 4–3 and $C^{18}O$ 3–2 were averaged by cloud, as shown in Figure 1. Unlike the individual source spectra, the cloud-averaged Perseus spectra show a secondary feature at 4.4 km s^{-1} on the blue side of the cloud-average V_{lsr} of 8.0 km s^{-1} in both lines. Four sources in the L1448 and L1455 regions taken together have an average V_{lsr} of 4.6 km s^{-1}, consistent with the weaker component of the Perseus spectra. One source, J032536.4+304523 (L1448-N), has the strongest HCO^+ 4–3 and fourth strongest $C^{18}O$ 3–2 integrated intensity of all sources in Perseus. The remaining 29 sources in Perseus have an average V_{lsr} of 7.8 km s^{-1} and make up the bulk of emission for the cloud-averaged spectra, consistent with the stronger component at higher velocity. Thus sources in the L1448 and L1455 regions are shifted in velocity with respect to the rest of the Perseus molecular cloud.

The Taurus cloud-averaged spectra are well-fit by a single Gaussian in both lines, with no indication of any blending of different velocity components of sources within the cloud. Given that the broad nature and double peak of the line in Perseus can be explained by blending, and no broadening is seen in Taurus, there is no evidence for significant outflow contribution to the HCO^+ 4–3 and $C^{18}O$ 3–2 molecular emission in the averaged central spectra of either cloud. Details of the fit properties for the cloud-averaged spectra are found in Table 2. Although the outflow component does not contribute much (typically $\lesssim$5%) to the on-source integrated HCO^+ 4–3 intensity, it is possible to map the outflows in the HCO^+ line wings, as shown by Walker-Smith et al. (2014). Their study maps regions of the Perseus cloud, therefore capturing outflow contribution on large scales. Here the mapping of individual sources restricts the identification of outflows to the immediate environment surrounding the YSOs. The possibility remains that off-source regions of the field of view exhibit broadening of the molecular line due to outflows. This is discussed further in Section 3.2.

3.2. Categorizing emission morphology

Examples of the reduced spectral maps are shown in Figure 2. All spectra have been resampled to 0.2 km s^{-1} velocity channels. Maps in HCO^+ 4–3 and $C^{18}O$ 3–2 are presented for a bonafide Stage I embedded source (J032837.1+311328, top) and a more evolved Stage II PMS with a disk (J032840.6+311756, bottom). The Stage I source exhibits centrally concentrated emission with no contamination from nearby sources or clouds in the field. In contrast, the Stage II source has widespread emission throughout the field.

The emission morphology can be categorized for all six wavelengths observed. $C^{18}O$ 3–2 serves as a tracer of the high column density environment within the cloud. HCO^+ 4–3 has a higher critical density (n_{crit} >10^6 cm^{-3}) and effectively probes the inner regions of the protostellar envelope. The morphology of integrated intensity maps for each of these molecular tracers provides a qualitative indication of their embedded nature. Sources with localized emission in HCO^+ 4–3 are good candidates for truly embedded protostars while a lack of emission in HCO^+ 4–3 may indicate a non-embedded source such as an edge-on disk. Accompanying peak temperature maps are

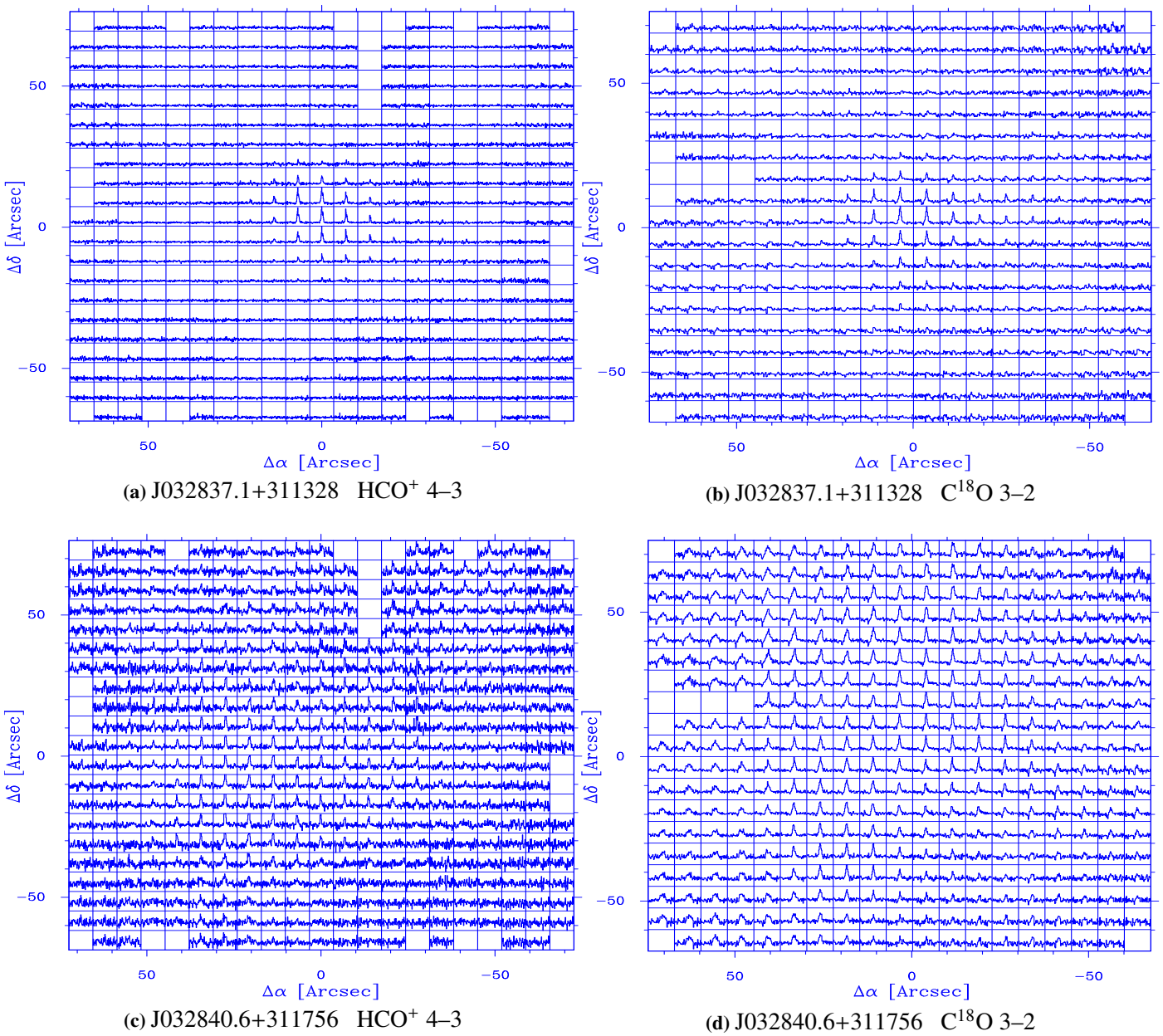

(a) J032837.1+311328 HCO^+ 4–3

(b) J032837.1+311328 $C^{18}O$ 3–2

(c) J032840.6+311756 HCO^+ 4–3

(d) J032840.6+311756 $C^{18}O$ 3–2

Fig. 2: Example of spectral maps obtained by the HARP instrument, visualized in Appendix C. The T_{mb} maximum value of the central spectrum dictates the scale of the y-axis in each map. *(a)* and *(b)* show the distribution of spectra for J032837.1+311328, a bonafide Stage I source (see Section 4.2) with central concentration of emission. *(c)* and *(d)* show the spectral map for a misfit source, J032840.6+311756, with widespread emission in both lines that result in a Stage II classification.

included to check for consistency with the morphology of the integrated intensity maps. For example, outflow emission would be revealed by more extended morphology in the integrated intensity maps compared to the peak temperature maps. The dust continuum morphology at 70 μm and 160 μm from PACS reveal warm dust originating from the region close to the protostar. 450 μm and 850 μm emission originates in the cooler parts of the outer envelopes and partially from surrounding cloud material.

Based on the morphology of the molecular line and dust continuum maps in Appendix C, which are cross-checked with the spectral maps such as shown in Figure 2, we define four distinct classes of emission. A first group has concentrated emission that peaks at the source position. Any emission offset of less than 5″ can be attributed to pointing inaccuracies. J032837.1+311328 in Figure 2 and Appendix C is a good example of a source with emission peaking on-source in both HCO^+ 4–3 and $C^{18}O$ 3–2 as well as each wavelength of dust continuum observations.

A second class has concentrated emission that is peaking off-source by more than 5–10″. Such an offset from the mid-IR position in HCO^+ 4–3 could be due to high density material in outflows or binarity, which would have a significant effect on the spectrally integrated intensity maps. J034350.9+320324 is an example of off-source emission in HCO^+ 4–3 due to binarity. Other examples include J032910.7+311820, J042110.0+270142, and J042111.4+270108. Molecular line emission in these sources is offset from the source position due to a companion within the same field of view. J042111.4+270108 has extended HCO^+ 4–3

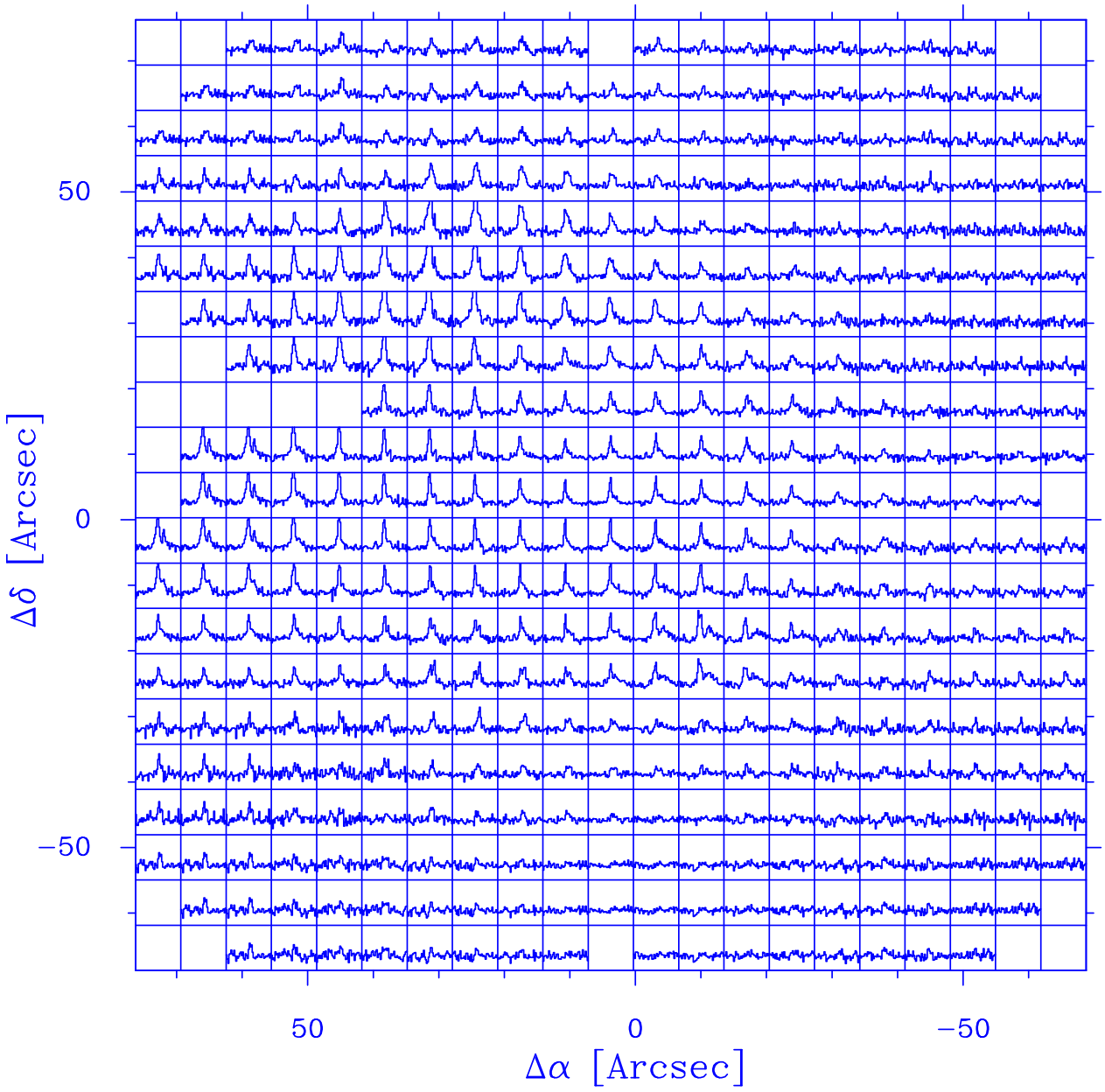

Fig. 3: HCO^+ 4–3 spectral map for J033314.4+310710 (B1-SMM3) showing evidence of outflow wings. Broadening of the line can be seen at low T_{mb} in the spectra off-source, e.g., the red wing visible at offsets of about (-20″, +10″). The central spectrum can be found in Appendix B.

throughout the field due to the presence of a third source in the mapped area, but with an off-source peak at the location of the binary companion. Identification of these binaries is described in further detail at the end of this section. The J034359.4+320035 HCO^+ 4–3 map has emission peaking significantly off-source as a result of another object seen in both molecular line and dust continuum emission (see Appendix A for more detail).

The third class has extended emission, where a peak may be observed but the emission is widespread within the field of view on scales of 20″ or more. Examples are J032839.1+310601 and J032840.6+311756, which show extended emission in both molecular lines and in SCUBA dust continuum maps. Several sources with extended HCO^+ 4–3 emission exhibit off-source line broadening in their spectral maps of order a few km s^{-1}, suggesting outflow activity. An example of a source with evidence for outflows, J033314.4+310710 (B1-SMM3), is shown in Figure 3. Though present, the weak outflow wings do not constitute a significant contribution to the integrated intensity. Therefore, a likely cause of the extended emission is contamination from another object in the field. J032859.5+312146, J032900.6+311200, J032901.6+312028, J032903.3+311555, J032951.8+313905, and J033320.3+310721 (B1-b) also have spectral maps that indicate a slight broadening of the line off-source. In J033314.4+310710 (B1-SMM3) and J033320.3+310721 (B1-b) the weak outflow wing can be seen in the central spectrum. In the case of J032859.5+312146, J032900.6+311200 and J032951.8+313905 there appear to be no other nearby YSOs or dense cores that might contaminate the field. The additional contribution from outflow wings alone is not enough to explain the widespread emission in these sources; there may be distributed high density cloud material

present in the field. J032901.6+312028, J032903.3+311555, J033314.4+310710 (B1-SMM3), and J033320.3+310721 (B1-b) all contain previously catalogued objects within their mapped regions that are likely causes of the extended emission (see Appendix A).

Finally, the fourth class consists of all non-detections down to rms noise levels.

These four groups are used to diagnose the morphology of emission for each source at each observed wavelength. The classification of emission for each source can be found in Table 3. Concentrated emission that is peaking on-source is indicated with a P, concentrated emission that is peaking off-source is indicated with an O, extended emission is indicated with an E, and a non-detection is indicated with an N. Subscripts for each of these classifications correspond to the emission bands: H is HCO^+ 4–3, C is $C^{18}O$ 3–2, 7 is 70 μm, 1 is 160 μm, 4 is 450μm and 8 is 850 μm.

Four binary sources are identified in the sample: J032910.7+311820, J034350.9+320324, J042110.0+270142, and J042111.4+270108. These are flagged as binaries based on their 70 μm morphology. The data at this wavelength has the highest spatial resolution and the dust it traces is warm enough to reveal the presence of two objects while emission at other wavelengths is too widespread to resolve two objects and appears as emission on a larger scale from a single object. The sources listed above show a secondary object within 20″ of the primary target.

4. Source Classification

4.1. Concentration factors

To quantitatively distinguish embedded sources from non-embedded disks or background features, we can set constraints on the concentration of HCO^+ 4–3 and 850 μm emission. In this section we aim to bring a quantitative definition to identify truly embedded, early-stage sources based on the degree of concentration in their emission. Previous studies of SCUBA 850 μm emission (Johnstone et al. 2001; Walawender et al. 2005) define the following concentration factor:

$$C_{850} = 1 - \frac{1.13B^2 S_{850}}{\pi R_{\rm obs}^2 F_0} \quad (1)$$

where B is the diameter of the instrument beam, $R_{\rm obs}$ is the radius of the source envelope in the same units as the beam size, S_{850} is the total 850 μm flux within $R_{\rm obs}$ in units of Jansky, and F_0 is the peak flux of the envelope in Jansky beam^{-1}. The 850 μm concentration factor gives an initial insight into the nature of the core. van Kempen et al. (2009) suggested that concentrated sources ($C_{850} > 0.75$) likely contain protostars while low concentration sources ($C_{850} < 0.40$) are unlikely to be embedded YSOs. In our calculations we determine $R_{\rm obs}$ by fitting a circular 2D Gaussian to the emission profile. $R_{\rm obs}$ is set equal to the FWHM of the Gaussian fit. In some cases masking was necessary to exclude contaminating emission or emission from nearby sources, in which case a mask radius was chosen with respect to the source position, and all points outside the mask were set to a representative background value. If the FWHM of the 2D Gaussian fit exceeded the masking radius, $R_{\rm obs}$ was set equal to the mask radius. To determine the flux, maps were converted to units of Jansky using a beam correction factor of $\pi(B/2)^2$ where $B = 23''$. This is larger than the main-beam size of the JCMT at this wavelength (∼15″) due to the data reduction methods and error beam corrections applied by Di Francesco et al. (2008). The SCUBA 850 μm concentration factors, total flux, peak flux, and envelope radii are listed in Table 3.

To identify whether these sources are truly embedded, we can apply the same formula to the HCO^+ 4–3 emission. Following a method similar to that described by van Kempen et al. (2009), Eq. 1 can be translated to a spectral map concentration parameter that is analogous to the calculation of the 850 μm concentration factor:

$$C_{\rm HCO^+} = 1 - \frac{1.13B^2 S_{\rm HCO^+}}{\pi R_{\rm obs}^2 S_{\rm HCO^+}^{\rm peak}} \quad (2)$$

where B and $R_{\rm obs}$ retain their previous definitions with $B = 15''$, the HARP beam size. $S_{\rm HCO^+}^{\rm peak}$ is the peak integrated intensity within the beam, and $S_{\rm HCO^+}$ is the spatially and spectrally integrated intensity $\int T_{\rm mb} {\rm d}V$ within $R_{\rm obs}$. To calculate $S_{\rm HCO^+}$, each integrated intensity map first has a beam correction applied in the same manner as the SCUBA maps, with a correction factor of $\pi(B/2)^2$ where $B = 15''$. The resulting concentration factors are given in Table 3.

Concentration factors at 850μm have been previously calculated using CLUMPFIND (Williams et al. 1994) in Perseus (Kirk et al. 2006, and references therein). About half of the sources have concentration factors consistent to within 20%, but some cases differ from the values reported here by up to 50%. These discrepancies can be attributed to the different methods used to determine $R_{\rm obs}$. CLUMPFIND extends the radius out to a predetermined sensitivity limit, often resulting in larger $R_{\rm obs}$ than that derived from the 2D Gaussian fits used here. Applying masks to exclude emission from nearby sources also has an effect on the $R_{\rm obs}$ determined from a 2D Gaussian fit. The 850 μm flux values reported in Di Francesco et al. (2008) agree with the S_{850} flux values presented in this paper to within 10%, which is within the flux uncertainties.

4.2. Evolutionary stages

Given our concentration factor definitions, we can apply a similar scheme for stage identification as van Kempen et al. (2009). The classification of an object depends on molecular line observations of HCO^+ 4–3 and $C^{18}O$ 3–2 as well as emission in the continuum, in particular the 850 μm SCUBA observations. Multi-wavelength observations are necessary for a proper classification of the Stage. Detection and concentration analysis of only HCO^+ 4–3 is not sufficient. For Stage I, both HCO^+ 4–3 and the 850 μm continuum must be detected within 5–10″ of the source position and show compact emission. The $C^{18}O$ 3–2 line may be compact or extended, but it must also be detected within a 5–10″ offset. Specifically, the following criteria are adopted for stage classification:

- Stage I:
  - HCO^+ 4–3 peaking on-source and/or contained entirely within the 15″ beam, with $C_{\rm HCO^+} > 0.6$ and $\int T_{\rm mb} {\rm d}V > 0.4$ K km s^{-1} *and*;
  - SCUBA emission at the source position that is not point-like *and*;
  - detection of $C^{18}O$ 3–2 at the source position.
- Stage II:
  - non-detection of HCO^+ 4–3 and SCUBA down to rms levels, or $C_{\rm HCO^+}$ and $C_{850} < 0.4$ *or*;

Table 3: Characterization of source emission, concentration factor parameters, and stage classifications based on JCMT HARP, JCMT SCUBA, and *Herschel* PACS spatial maps.

	Code[a]	S_{850}[b] [Jy]	F_0^{850} [Jy beam^{-1}]	C_{850}	R_{obs}^{850c} [″]	S_{HCO^+}[d] [K km s^{-1}]	$S_{HCO^+}^{peak}$ [K km s^{-1} beam^{-1}]	C_{HCO^+}	$R_{obs}^{HCO^+c}$ [″]	Stage
J032522.3+304513	P_{HC7148}	2.9	1.4	0.67	35	14.1	4.7	0.65	25	I
J032536.4+304523	P_{HC7148}	11.0	5.4	0.61	32	160	17.6	0.63	45	I
J032637.4+301528	P_{HC7148}	0.82	0.37	0.60	32	8.2	1.4	0.69	40	I
J032738.2+301358	P_{H148} E_C N_{71}	0.50	0.29	0.48	25	10.4	2.8	0.66	30	I
J032743.2+301228	P_{H7148} E_C	1.2	0.53	0.30	25	5.5	3.6	0.71	21	I
J032832.5+311104	P_{H145} N_{C7}	1.3	0.30	0.47	40	7.3	3.6	0.61	21	I
J032834.5+310705	P_{148} N_{HC7}	0.36	0.31	0.72	28	–	–	–	–	C
J032837.1+311328	P_{HC7148}	1.7	0.87	0.59	30	12.5	5.2	0.61	22	I
J032839.1+310601	E_{HC148} N_7	1.3	0.35	0.22	30	10.8	1.0	0.45	40	II
J032840.6+311756	E_{HC148} N_7	2.0	0.66	0.41	40	24.0	2.4	0.49	40	II
J032845.3+310541	P_{HC71} E_{48}	0.75	0.26	0.35	30	4.5	1.6	0.62	25	I
J032859.5+312146	O_{48} E_{HC} N_{71}	3.6	1.3	0.42	30	92.0	11.9	0.61	40	I
J032900.6+311200	P_{7148} E_{HC}	0.33	0.34	0.71	25	21.0	3.7	0.62	35	I
J032901.6+312028	P_{71} E_{HC48}	7.3	2.1	0.45	35	179	25.2	0.70	44	C
J032903.3+311555	P_{4871} E_{HC}	10.3	4.8	0.56	30	74.0	19.4	0.62	29	I
J032904.0+311446	E_{HC48} N_{71}	3.6	1.1	0.31	30	40.2	10.4	0.50	25	C
J032910.7+311820[B]	O_{HC7148}	6.9	1.8	0.64	45	69.7	9.2	0.63	32	I
J032917.2+312746	P_{HC7148}	1.1	0.48	0.63	36	15.3	4.4	0.73	32	I
J032918.2+312319	O_{7148} E_{HC}	1.3	0.60	0.53	30	19.9	2.6	0.64	35	I
J032923.5+313329	P_{H71} O_C	–	–	–	–	9.7	1.6	0.66	37	I
J032951.8+313905	P_{718} O_4 E_{HC}	1.1	0.49	0.63	35	20.9	4.5	0.65	33	I
J033121.0+304530	P_{HC7148}	1.9	1.3	0.62	27	11.8	4.1	0.68	27	I
J033218.0+304946	P_{C7148} O_H	3.4	2.5	0.60	26	23.4	5.2	0.63	31	I
J033313.8+312005	O_8 E_{H14} N_{C7}	2.0	0.39	0.46	42	5.5	0.9	0.68	39	C
J033314.4+310710	P_{71} E_{HC48}	7.0	1.2	0.30	40	33.0	3.0	0.45	40	C
J033320.3+310721	O_{148} E_{HC} N_7	5.4	1.2	0.57	45	32.1	4.2	0.62	40	C
J033327.3+310710	P_{H7148} E_C	1.2	0.37	0.29	30	7.9	2.1	0.65	30	I
J034350.9+320324[B]	P_{7148} O_H E_C	2.9	0.7	0.37	35	20.9	5.3	0.73	35	I
J034356.9+320304	P_{H7148} E_C	2.7	1.7	0.65	30	28.4	6.9	0.69	33	I
J034357.3+320047	P_H O_{7148} E_C	5.6	2.2	0.62	36	20.9	8.5	0.65	24	I
J034359.4+320035	O_{H7148} E_C	–	–	–	–	–	–	–	–	C
J034402.4+320204	P_7 E_{HC481}	2.1	0.61	0.27	30	27.7	5.2	0.52	30	C
J034443.3+320131	O_{HC7148}	1.8	1.0	0.63	31	27.3	12.2	0.62	22	I
J034741.6+325143	P_{C71} O_H	–	–	–	–	5.1	3.2	0.65	19	I
J041354.7+281132	P_{7148} N_{HC}	0.28	0.19	0.56	25	–	–	–	–	II
J041412.3+280837	P_{71} N_{HC}	–	–	–	–	–	–	–	–	II
J041534.5+291347	P_{71} N_{HC}	–	–	–	–	–	–	–	–	II
J041851.4+282026	P_{71} E_C N_H	–	–	–	–	–	–	–	–	II
J041942.5+271336	P_{H7148} E_C	1.7	0.68	0.62	36	9.4	4.0	0.64	23	I
J041959.2+270958	O_{H7148} E_C	2.2	0.67	0.62	41	39.3	4.1	0.61	45	I
J042110.0+270142[B]	P_7 E_{HC1}	–	–	–	–	13.3	1.5	0.42	35	II
J042111.4+270108[B]	P_{71} O_H E_C	–	–	–	–	9.8	3.2	0.63	26	C
J042656.3+244335	P_{C718} O_H N_4	0.85	0.36	0.29	25	1.5	0.9	0.43	15	II
J042757.3+261918	P_{H71} E_{C48}	0.55	0.21	0.58	34	16.6	2.3	0.66	41	I
J042838.9+265135	P_{H7148} E_C	6.1	0.64	0.49	60	5.6	3.8	0.69	20	I
J042905.0+264904	P_7 O_1 N_{HC}	–	–	–	–	–	–	–	–	II
J042907.6+244350	P_{71} N_{HC}	–	–	–	–	–	–	–	–	II
J042923.6+243302	P_{H71} E_C	–	–	–	–	27.2	5.0	0.66	36	I
J043150.6+242418	P_{71} N_{HC}	–	–	–	–	–	–	–	–	II
J043215.4+242903	P_{718} N_{HC4}	–	–	–	–	–	–	–	–	II
J043232.0+225726	P_{7148} N_{HC}	0.39	0.34	0.61	23	–	–	–	–	II
J043316.5+225320	P_{H7148} N_C	0.67	0.56	0.55	23	2.2	2.2	0.52	13	II
J043535.0+240822	P_{718} E_{HC} N_4	0.22	0.20	0.66	25	7.1	1.7	0.45	25	II
J043556.7+225436	N_{HC71}	–	–	–	–	–	–	–	–	II
J043953.9+260309	P_{HC7148}	7.9	1.8	0.65	49	87.5	14.7	0.67	38	I
J044138.8+255626	P_{7148} N_{HC}	0.13	0.10	0.65	29	–	–	–	–	II

Notes.
Sources marked with B superscript indicate a visible binary or multiple system based on PACS 70 μm data.
[(a)] Emission classification: P = peaking on-source, O = offset peaking, E = extended emission, N = non-detection. Subscript identifiers: H = HCO^+ 4–3, C = $C^{18}O$ 3–2, 7 = 70 μm, 1 = 160 μm, 4 = 450 μm, 8 = 850 μm
[(b)] Fluxes for 850 μm were derived using a 23″ beam.
[(c)] R_{obs} was derived from the FWHM of a circular 2D Gaussian fit to the source emission.
[(d)] Spatially and spectrally integrated intensities for HCO^+ 4–3 were derived using a 15″ beam.

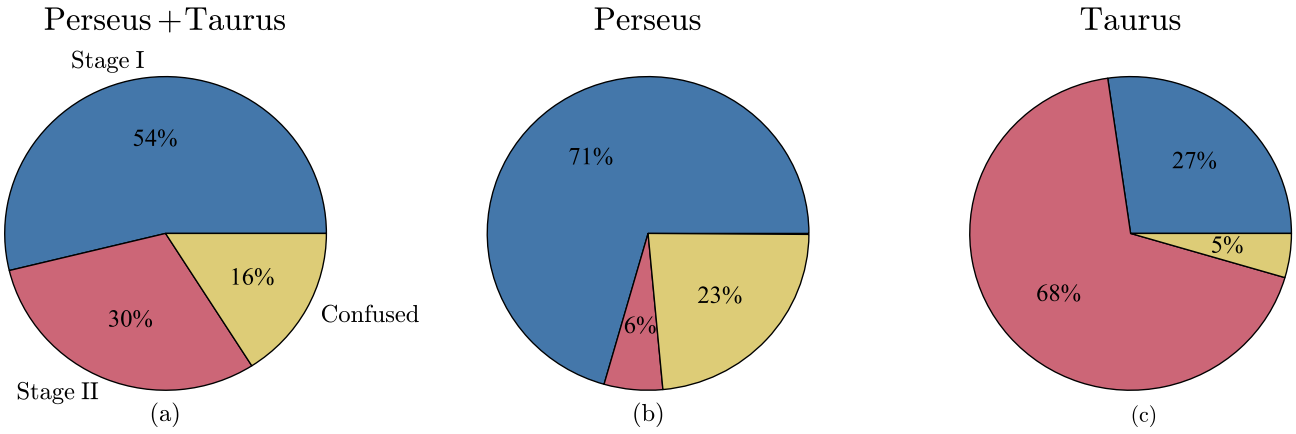

Fig. 4: Statistics for stage classification. Stage I embedded objects are shown in light blue, Stage II objects are shown in light red, Confused objects are shown in yellow. *(a)* The entire sample observed in HCO^+ 4–3 and $C^{18}O$ 3–2 from the Perseus and Taurus clouds: 56 sources. *(b)* Statistics for only the Perseus cloud: 34 sources. *(c)* Statistics for only the Taurus cloud: 22 sources.

  - non-detection of $C^{18}O$ 3–2 down to rms levels, or no variation of $C^{18}O$ 3–2 on scales of 30″ *or*;
  - point-like emission in all continuum bands.
- Confused:
  - HCO^+ 4–3, SCUBA, and $C^{18}O$ 3–2 peaking at an offset of 20″ or more from source position.

In order to be classified as Stage I, a source must meet all of the Stage I criteria; partially meeting the requirements is not sufficient. The concentration factor criteria adopted here are less strict than those defined in van Kempen et al. (2009).

To motivate our criteria for HCO+, it is useful to compare with models of the line emission as a function of evolutionary stage. This has been done by Hogerheijde et al. (1997, see Figure 6 in their paper) using the same type of Shu (1977) collapse model that was used to model the changes in continuum SEDs with evolution. Both the spatial extent and integrated envelope intensities of multiple HCO^+ lines were modeled using the full non-LTE excitation and radiative transfer code RATRAN (Hogerheijde & van der Tak 2000). For a constant HCO^+ abundance of 1.2×10^{-8} they find that HCO^+ 4–3 emission during the Stage I lifetime ($\lesssim$ few$\times10^5$ yr) can be expected on spatial scales of $\sim 30-60''$ for sources in Taurus. This number will be up to a factor of two lower for sources in the more distant Perseus cloud, but is consistent with the scales on which the majority of Stage I sources in this paper are fitted by concentration factor analysis. As the Shu collapse model evolves in time toward Stage II, the HCO^+ 4–3 FWHM of emission from the source drops drastically, near to the 14″ beam size with which the predictions were convolved, which is consistent with the beam size of the JCMT.

The same models show that the expected integrated envelope intensities for HCO^+ 4–3 within Stage I lifetimes are on the order of 10-20 K km s^{-1} and drops to ∼5 K km s^{-1}. These values are in the same range or somewhat larger than our observed intensities, but the model values depend on the adopted HCO+ abundance.

Another comparison can be made with models of HCO^+ 4–3 and $C^{18}O$ 3–2 emission from the deeply embedded source IRAS 2A located in NGC 1333 using RATRAN as presented in San-Jose Garcia, et al. (subm.). They also use a constant abundance profile for HCO^+ 4–3 whereas that for $C^{18}O$ 3–2 takes freezeout onto grains into account at lower temperatures. The same analysis as described in Section 4.1 is applied to both lines. The 2D Gaussian fits result in R_{obs} values of 21″ and 26″ for HCO^+ 4–3 and $C^{18}O$ 3–2, respectively. Concentration factors are $C = 0.58$ for both lines. These are taken as indicative values for an embedded YSO in the analysis of our observed sample.

Based on the expected scale and intensity of the HCO^+ 4–3 and 850 μm emission, a concentration factor $C > 0.6$ is sufficient to classify a source as a Stage I embedded object. The integrated intensity limit on HCO^+ 4–3 of 0.4 K km s^{-1} is derived from observations of Stage II sources with disks where, due to beam dilution, the disk emission in a 15″ beam is generally well below this limit, of order 0.1 K km s^{-1} (e.g., Thi et al. 2004).

Applying these definitions to the observed sample, 30 out of 56 sources (54%) are Stage I deeply embedded protostars, 17 (30%) are Stage II classical T Tauri stars with a surrounding disk, and 9 sources (16%) remain confused based on a morphology in gas and dust emission that does not cleanly fit the criteria for Stage I or Stage II. These statistics include all sources in both Perseus and Taurus. Sources in Serpens could not be classified as they were only observed in $C^{18}O$ 3–2.

Separating the classifications by cloud reveals that Perseus contains a higher percentage of embedded sources than Taurus. Out of the 34 sources in Perseus, 24 (71%) are bonafide Stage I, 2 (6%) are Stage II, and 8 (23%) are confused sources. Of 22 sources in Taurus, 6 (27%) are classified as Stage I, 15 (68%) are Stage II, and 1 (5%) is confused. These statistics are represented in Figure 4.

All sources with emission at all wavelengths that fall under the on-source centrally concentrated observational category outlined in Section 3.2 (i.e., P_{HC7148}) are identified as bonafide Stage I sources using the concentration factor method. For the entire sample there is only a single object, J043316.5+225320, that shows HCO^+ 4–3 peaking on-source (P_H) but falls under the Stage II category due to low concentration factors for 850 μm and HCO^+ 4–3, and non-detection in $C^{18}O$ 3–2. Thus, centrally concentrated on-source HCO^+ 4–3 emission is a good qualitative indicator that the object is a truly embedded YSO. Five of the eight confused sources have widespread emission in both molecular lines and SCUBA dust continuum emission (E_{HC48}) and often contain a peak within the extended emission that is offset from the source position. The three remaining confused sources are classified as such for different reasons − further explanation can be found in Appendix A.

Stage II sources either exhibit a morphology that is extended in HCO^+ 4–3 and $C^{18}O$ 3–2 with no clear peak in emission, thus resulting in a low concentration factor, or there is no detection

in either molecular line (N_{HC}). Non-detection of both molecular lines suggests an evolved PMS star with a disk. One example is the case of IRS63 in Oph, where previous interferometric data of HCO^+ with the Sub-Millimeter Array (SMA) have revealed a disk (Lommen et al. 2008; Brinch & Jørgensen 2013). The integrated intensity in HCO^+ 3–2 when convolved with the JCMT beam is 0.28 K km s^{-1} and originates mostly from the disk (van Kempen et al. 2009). Due to the weak HCO^+ 4–3 contribution and small size of the emitting region in disks, the signal is beam-diluted below the sensitivity limit of the single-dish JCMT observations.

It should be noted that there are two caveats when relying on the presence of a central peak in the HCO^+ spatial map for Stage I identification: HCO^+ may be optically thick which may prevent a peak; and CO, the precursor of HCO+, may be frozen out in the lowest luminosity and/or coldest sources. Models of NGC 1333 IRAS 2A, one of the strongest HCO^+ sources, demonstrate that both issues do not largely affect the results.

4.3. HCO^+ infall signatures

The presence of a blue-dominated asymmetry in the line profile of a HCO^+ single pointing observation is often used to provide strong evidence of infall of dense material from the outer envelope (Gregersen et al. 1997; Mardones et al. 1997; Myers et al. 2000). Three sources in Taurus are identified as having such an asymmetry in their central spectra contained within the 15″ JCMT beam (see Section 3.1). All three are found to be Stage I sources according to the concentration factor method presented here.

Other sources show interesting line profile shapes with a blue-dominated excess and self-absorption at the source velocity of the spectrum. These include J032837.1+311328, J032904.0+311446 (HH 7-11), J032951.8+313905, J033121.0+304530, J033218.0+304946, and J034443.3+320131. Five of the six sources are classified as Stage I in this paper, with J032904.0+311446 (HH 7-11) classified as confused due to the widespread HCO^+ 4–3 emission in the field, which may explain its irregular line profile. Overall, spectrally resolved line profile asymmetries are not frequently observed and therefore infall signatures cannot be used for widespread confirmation of the Stage I nature YSOs. Multiwavelength spatial maps provide the strongest technique thus far to characterize YSOs.

4.4. HCO^+ single pointing vs. mapping

Other attempts are being made to determine the evolutionary stage of YSOs with HCO^+. A study by Heiderman & Evans (2015) has classified YSOs based solely on the detection of HCO^+ 3–2 at the source position without the aid of spatial mapping. It is useful to test the robustness of this method of classification by comparing our own central spectra detections in HCO^+ 4–3 to the stages determined via the concentration factors. Based on the HCO^+ 4–3 spectra extracted from the source position, shown in Appendix B, and the spectral characteristics listed in Table 1, our sample consists of 43 detections out of the 56 objects in Perseus and Taurus.

Based on the concentration factor criteria of HCO^+ 4–3, 32 out of 56 sources in our sample are Stage I, leaving many sources that would be misidentified using the detection-only method. Some of these are Stage II sources in our assignment, others have low concentration factors or have emission that is offset by 20″ or more away from the source position.

Based on the comparison of central spectrum detection to concentration factor classification in our sample, there are likely to be misassignments on the order of 20–30% in the identification of Stage I embedded sources if only the detection of HCO^+ is applied as an indicator of protostellar stage. A single pointing detection cannot properly characterize the YSO, thus a detection-only sample is likely to introduce a bias that will overestimate the number of Stage I sources and thus also their lifetime. This point is discussed further in Section 4.7.

4.5. Correlations

Trends between the two observed molecular lines and 850 μm dust emission may give insight into the relative amounts of high (column) density gas and cool dust that are present in Stage I and Stage II sources. Figure 5 shows three different correlation plots between these tracers. Pearson correlation coefficients are calculated for each comparison using only Stage I detections. The significance of each correlation is calculated in terms of $\sigma_P = |r|\sqrt{n-1}$, for a correlation coefficient r and sample size n (Marseille et al. 2010). Molecular line integrated intensities are taken from the central spectra of the source and are therefore contained within a 15″ beam whereas the 850 μm flux values are taken from concentration factor analysis as described in Section 4.1 and apply to a somewhat larger 23″ beam.

The top panel shows the HCO^+ 4–3 integrated intensities versus the 850 μm flux for all sources where both tracers are detected. These values are found to be strongly correlated, with a significance of $4.6\sigma_P$. Such a correlation can be expected, particularly for Stage I sources. More envelope material, as traced by the cooler dust emission at 850 μm, suggests that there will be a larger number of molecules present in the gas phase for embedded protostars, assuming that the gas and dust are well coupled and that the abundance of the molecule is constant throughout this region. All Stage II sources with $3\sigma_I$ detections in HCO^+ 4–3 have low intensity ($\leq$ 1.3 K km s^{-1}). Though the numbers are small, it is interesting to note that for positive detections the HCO^+ 4–3 intensity remains relatively flat while 850 μm flux varies by an order of magnitude for Stage II sources. This cannot be used as a threshold for separation of Stage I and Stage II, however, as there are Stage I sources that share these low HCO^+ 4–3 intensities. Spatial maps are therefore a requirement for proper identification.

Note that for Stage I sources, some fraction of the continuum emission (~20–80%, Hogerheijde et al. 1997; Jørgensen et al. 2009) originates from the disk rather than the envelope whereas the majority of the line emission originates in the envelope. The variable disk continuum contribution will tend to lower the correlation.

$C^{18}O$ 3–2 integrated intensity and 850 μm flux also show a positive correlation with a $3.3\sigma_P$ significance. Flux for Stage II sources here generally remain low in both $C^{18}O$ 3–2 and 850 μm. Several Stage I sources also share these low intensity and flux values, but only Stage I or confused sources are found with $C^{18}O$ 3–2 intensity $\gtrsim$ 2.0 K km s^{-1}. The $C^{18}O$ 3–2 versus HCO^+ 4–3 trend in the bottom panel of Figure 5 is well correlated ($4.2\sigma_P$). In this plot the Stage II sources are most tightly grouped around low HCO^+ 4–3 and $C^{18}O$ 3–2 intensities, with only a few Stage I or confused sources of comparable low intensity for both lines. These plots indicate that HCO^+ 4–3 is indeed the best tracer for Stage I identification and that an HCO^+ 4–3 intensity

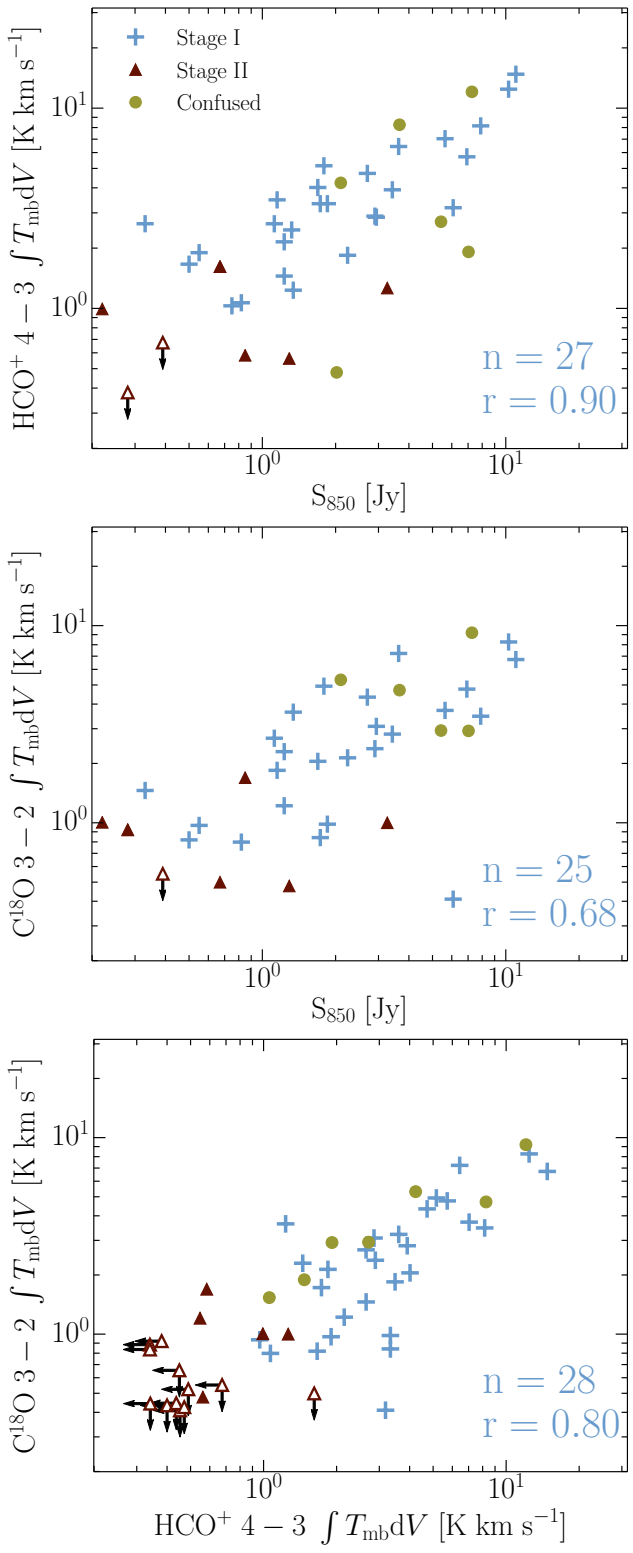

Fig. 5: Molecular line intensity and dust continuum flux correlations. Integrated intensities for spectral lines are taken from the central spectrum of each source. Flux values at 850 μm are taken from concentration factor analysis. Stage I (blue cross), Stage II (red triangle), and Confused (yellow circle) sources are shown. Upper limits are shown in hollow markers with black arrows indicating the bounds. Sample size and Pearson correlation coefficient for Stage I sources are given in the lower-right corner of each plot. Serpens sources are excluded. *Top:* HCO^+ 4–3 versus 850 μm flux *Middle:* $C^{18}O$ 3–2 versus 850 μm flux *Bottom:* $C^{18}O$ 3–2 versus HCO^+ 4–3.

threshold of $\gtrsim$0.6 K km s^{-1} will result in a majority of Stage I sources being correctly identified. However, spatial mapping is still needed to properly classify those sources with HCO^+ 4–3 intensity above this threshold but with low spatial concentration.

4.6. Comparison to other studies

4.6.1. Perseus sources

Table 4: Properties of Perseus sources – HCO^+ 3–2, and H_2O obseravations in other studies

Object	Stage[a]	Stage I?[b]	PACS H_2O?[c]
J032522.3+304513	I	-	Y
J032536.4+304523	I	-	Yc[d]
J032637.4+301528	I	-	N
J032837.1+311328	I	-	Y
J032900.6+311200	I	Y	-
J032901.6+312028	C	-	Ye[e]
J032904.0+311446	C	Y	-
J032910.7+311820	I	Y	Yc[d]
J032917.2+312746	I	Y	-
J032918.2+312319	I	Y	-
J032923.5+313329	I	Y	-
J032951.8+313905	I	Y	N
J033121.0+304530	I	Y	Y
J033218.0+304946	I	Y	N
J033313.8+312005	C	N	-
J033314.4+310710	C	Y	N
J033320.3+310721	C	Y	-
J033327.3+310710	I	Y	Y
J034356.9+320304	I	-	Ye[e]
J034443.3+320131	I	-	Ye[e]

Notes. [(a)] Classification in this paper. [(b)] Classification from Heiderman & Evans (2015) based on single pointing detection of HCO^+ 3–2. [(c)] Detection of the H_2O ($2_{12} - 1_{01}$) 179.527μm line from *Herschel* PACS observations (Karska et al. 2014). [(d)] Source map is contaminated by emission from other nearby sources. [(e)] Emission is extended and associated with the target source.

The source sample observed in HCO^+ 3–2 and classified by Heiderman & Evans (2015) has 13 sources in common with our sample. Though it is a small subset from Perseus, comparing their classification to our assignments provides a first look at how well the single pointing detection method matches with the spatial map concentration factor method. Note that for single pointings the only requirement for a Stage I source classification is based on the detection criterion $\int T_{\rm mb} dV \geq 0.68$ K km s^{-1} for the HCO^+ 3–2 line in a 28″ beam, which is more conservative than our integrated intensity criterion for HCO^+ 4–3. There is no effort to identify the source specifically at another stage. Table 4 shows the common sources and designations from each study.

For every source in Table 4 that is assigned a Stage I classification in this paper, Heiderman & Evans (2015) also report a confirmed Stage I source from their HCO^+ 3–2 data. Note that they define an earlier Stage 0, but make no distinction between Stage 0 and Stage I sources observationally. No such distinction is made in this paper. Stage I encompasses the entire embedded phase of the YSO. Four differences arise from this comparison. J032904.0+311446 (HH 7-11 MMS6), J033314.4+310710 (B1-SMM3), and J033320.3+310721 (B1-b) are identified as confused sources in this work due to their emission morphology (see

Table 5: Properties of Taurus sources – color criteria, HCO^+ 3–2, and H_2O obseravations in other studies

Object	Stage[a]	Embedded/Visible[b]	HCO^+ 3–2?[c]	PACS H_2O?[d]
J041354.7+281132	II	Embedded	N	–
J041959.2+270958	I	Embedded	Y	Y
J042110.0+270142	II	Embedded	Y	–
J042111.4+270108	C	–	–	Y
J042656.3+244335	II	Embedded	Y	–
J042757.3+261918	I	Embedded	Y	Y
J042907.6+244350	II	–	–	Y
J042923.6+243302	I	Embedded+Visible	Y	–
J043150.6+242418	II	Visible	N	–
J043215.4+242903	II	Visible	N	–
J043232.0+225726	II	Embedded	N	–
J043316.5+225320	II	Embedded	N	–
J043535.0+240822	II	Embedded	Y	Y
J043953.9+260309	I	Embedded	Y	–

Notes. [(a)] Classification in this paper. [(b)] Classification taken from Hogerheijde et al. (1997) based on a flux- and color-limited sample. [(c)] Detection of HCO^+ 3–2 within a 19″ beam (Hogerheijde et al. 1997). [(d)] Detection of the H_2O ($2_{12} - 1_{01}$) 179.527μm line from *Herschel* PACS observations (Mottram et al., in prep.).

Section 4.2) while they are identified as Stage I sources in Heiderman & Evans (2015). J033313.8+312005 is also identified as confused in this work, though it may be closer to Stage II (see Appendix A). Heiderman & Evans (2015) report no detection of HCO^+ 3–2 in their observations of this source and conclude that it is not Stage I. The two methods are both effective and mostly consistent for this given subset, but spatial mapping is needed for information about the environment surrounding the source in order to confirm the Stage I assignment.

Karska et al. (2014) present *Herschel* PACS spectral maps of 22 sources in the Perseus molecular cloud as part of the "William *Herschel* Line Legacy" (WILL) survey (Mottram et al., in prep.), including 13 in common with the sample studied in this paper. Table 4 indicates that the H_2O ($2_{12} - 1_{01}$) 179.527μm transition was detected within the PACS central (~9.5″×9.5″) spaxel for four Stage 1 sources while three show no detection. The confused source J033314.4+310710 (B1-SMM3) also lacks detection. A further two Stage I sources, J034356.9+320304 (IC 348-MMS) and J034443.3+320131, and one confused source, J032901.6+312028, all show H_2O ($2_{12} - 1_{01}$) emission extending outside of the PACS central spaxel, but still associated with the source. Water emission from J032536.4+304523 (L1448-N) and J032910.7+311820 are both confused by nearby sources. In this paper J032910.7+311820 is marked as a binary source, with dominant emission offset to the northeast of the target source, which is consistent with the location of contaminating H_2O ($2_{12} - 1_{01}$) emission. There is no such similarity for J032536.4+304523 (L1448-N). Overall there does not seem to be a clear relationship between the Stage I classification of sources presented here and the nature of H_2O ($2_{12} - 1_{01}$) emission from the same sources.

4.6.2. Taurus sources

Several Taurus sources in this paper have previously been classified based on a simpler identification scheme. The sample presented in Table 5 was taken from Tamura et al. (1991), where they used a flux- and color-limited sample of IRAS point sources with the following selection criteria: $\log(F_\nu(25\,\mu\mathrm{m})/F_\nu(60\,\mu\mathrm{m})) < -0.25$, and $F_\nu > 5$ Jy at either 60 or 100μm. These color criteria were used to determine if the object was optically visible or embedded. Hogerheijde et al. (1997) performed single pointing observations of HCO^+ 3–2 towards these sources and analyzed only those with the strongest line intensities. Table 5 provides the stage classification given in this paper, the color criteria classification, and whether or not HCO^+ 3–2 was detected within a 19″ beam. All detections marked 'Y' have integrated intensities greater than the Heiderman & Evans (2015) threshold, and all but J042656.3+244335 have $\int T_{\mathrm{mb}} dV > 1.0$ K km s^{-1}. Therefore, these sources would be identified as embedded Stage I sources. All sources marked 'N' indicate no detection in HCO^+ 3–2 and would be classified as Stage II sources using the Heiderman & Evans (2015) threshold.

It is immediately clear that the color criteria definitions are highly inconsistent with the method of stage classification presented here. Out of 13 sources, nearly half would be incorrectly identified as embedded when they are in fact Stage II evolved PMS stars with disks. The detection of HCO^+ 3–2 is a better match, but discrepancies remain. J042110.0+270142, J042656.3+244335, and J043535.0+240822 are indeed detected above the $3\sigma_I$ limit in the central spectra of the HCO^+ 4–3 data presented here, but their spatial maps reveal that the emission is not well concentrated. These three sources are assigned a Stage II classification despite detection in HCO^+ 4–3. As with the Heiderman & Evans (2015) comparison, the comparison for a small sample in Taurus reinforces the need for spatial maps to characterize the environment and prevent improper identification of truly embedded sources. Similar to the central spectra versus spatial map test in Section 4.2, the difference in Taurus assignments shows that there is approximately 20–30% error in classification if only single pointing observations are used.

Six sources in Taurus overlap with the WILL sample observed with *Herschel*. Five of these have PACS detections of the 179.527μm water line on-source or within one spaxel offset (see Table 5, also Karska et al., in prep.). J042110.0+270142 and J042757.3+261918 are Stage I embedded YSOs, J042907.6+244350 and J043535.0+240822 are Stage II objects, and J042111.4+270108 remains confused. J043232.0+225726 is the sixth source in common, a Stage II object, but was not observed with PACS. No water lines were detected in the *Herschel* HIFI observations of this source (Mottram et al., in prep.). As with the sample in Perseus, there is no

clear trend between the Stage of the YSO and the presence of water emission.

There are two possible reasons for this lack of correlation. First, water traces the currently shocked gas where the jet or wind impacts on the envelope, rather than the quiescent envelope or entrained outflow material (Kristensen et al. 2012; Mottram et al. 2014). Second, some water emission can arise from the disk rather than the shocks (Riviere-Marichalar et al. 2012; Fedele et al. 2013).

4.6.3. Near-IR veiling as a diagnostic

An independent diagnostic of evolutionary stage can be provided by optical and near infrared spectroscopy of the young stars themselves rather than their surroundings. This technique is limited to the more evolved stages when the young (PMS/proto) star is actually visible. Large veiling indices $r_\lambda = F_{\rm excess}/F_{\rm star}$ are thought to be indicative of high mass accretion rates. At K-band, r_K indices > 2 identify sources as likely Stage I objects whereas $r_K < 1$ is characteristic of Stage II sources (Greene & Lada 1996).

As a proof of concept, we compare the sample of van Kempen et al. (2009) in Ophiuchus with that of Greene & Lada (1996) and Doppmann et al. (2005). The 11 overlapping sources are: GSS 30, WL12, WL 17, Elias 29, WL 19, WL 6, IRS 43, IRS 44, IRS 51, IRS 54, IRS 63. Except for IRS 51 and 63, all sources have infrared veiling indices $r_K > 2.0$ whereas IRS 51 and 63 have 1.8 and 1.7 respectively. All sources in the overlapping sample are classified as Stage I by van Kempen et al. (2009) except IRS 51, which is listed as an obscured disk, and WL 19 which is classified as confused. Doppmann et al. (2005) derive a veiling of 3.7 for WL 19 establishing its nature as a likely Stage I object. This good agreement provides further support for our classification scheme.

For Taurus, high resolution optical spectra have been obtained by White & Hillenbrand (2004) and Connelley & Greene (2010). The sources which overlap with our sample are summarized in Table 6. The fact that White & Hillenbrand (2004) could detect and obtain high resolution optical spectra for only half of the Class I Taurus sources already suggests a bifurcation in source types, with the optically visible sources closer to Stage II. The low veiling excesses at R-band found for most sources by White & Hillenbrand (2004), coupled with their low accretion rates (see below), indeed suggests that all these overlapping sources in Table 6 are Stage II objects. This is largely consistent with our classification, except that their sources with the highest r_R values –IRAS04248+2612 and GV Tau– are found to be Class I by our classification. The comparison with Connelley & Greene (2010) shows a mixed picture, partly because of the large uncertainties in many of their low r_K values which could make them consistent with both Stage I and II based on a division line around $r_K = 1 - 2$.

Another diagnostic of evolutionary stage could be mass accretion rates derived from spectroscopic features such as Hα equivalent widths. Indeed, Greene & Lada (1996) estimate the accretion rates for their Class I sources in Oph to be $\sim 10^{-6}$ M$_\odot$ yr^{-1}, higher than those for Stage II objects at $\sim (0-3)\times 10^{-7}$ M$_\odot$ yr^{-1}. However, White & Hillenbrand (2004) find no difference in mass accretion rates between their Class I and II sources. Table 6 shows that the few Stage I sources in our classification do not have systematically higher mass accretion rates than the other sources. Although source selection can play a role, a similar lack of difference between embedded and optically visible sources was found by Salyk et al. (2013) who compared mass accretion rates derived from Pfund β lines. The known variability and episodic nature of the accretion process (e.g., Kenyon & Hartmann 1987; Evans et al. 2009; Vorobyov & Basu 2015) may be largely responsible for this lack of a systematic trend.

Overall, our finding that a high fraction of Class I sources in Taurus display properties more similar to Stage II objects is consistent with earlier conclusions based on optical spectroscopy.

Table 6: Veiling indices and mass accretion rates derived from optical spectroscopy in Taurus

Object	Stage[a]	Veiling index		log $\dot{M}_{\rm acc}$[d]
		r_K[b,c]	r_{8400}[d]	
				[M$_\odot$/yr]
J034741.6+325143	I	high	-	-
J041354.7+281132	II	$0.12^{+1.08}_{-0.0}$	-	-
J041851.4+282026	II	-	<0.19	-7.36
J041959.2+270958	I	$0.60^{+1.20}_{-0.24}$	-	-
J042110.0+270142	II	$0.24^{+0.00}_{-0.24}$	-	-
J042111.4+270108	C	$0.00^{+1.44}_{-0.00}$	-	-
J042656.3+244335	II	high	-	-
J042757.3+261918	I	$0.00^{+2.76}_{-0.00}$	0.60±0.21	-8.97
J042905.0+264904	II	-	0.57±0.26	-6.79
J042923.6+243302	I	-	1.1±0.4	-6.71
J043215.4+242903	II	$0.12^{+2.52}_{-0.00}$	0.26±0.08	-7.54
J043150.6+242418	II	-	0.24±0.06	-7.65
J043232.0+225726	II	$0.54^{+1.08}_{-0.30}$	-	-
J043556.7+225436	II	-	<0.07	-8.50
J043535.0+240822	II	high	-	-
J044138.8+255626	II	-	<0.04	-8.11

Notes. [b] Classification in this paper. [b] Sources with r_K>2 are considered Stage I, those with $r_K < 1$ as Stage II. [c] Connelley & Greene (2010). [d] White & Hillenbrand (2004).

4.7. Stage I lifetime

Heiderman & Evans (2015) find that 84% of sources in their observed Class 0+I and Flat SED sample are true Stage I embedded objects based on their HCO$^+$ 3–2 single pointing criteria. They propose an updated timescale for Stage I sources (Stage 0+I in their notation) of 0.54 Myr, assuming a Class II lifetime of 2 Myr (see Section 4.4 and Table 3 in their paper). In Section 4.4 of this paper it was shown that the HCO$^+$ single pointing method may still result in ~30% overestimate of the number of Stage I objects, implying that the updated value of Stage I lifetime may be overestimated by as much as 30%.

Reevaluation of the lifetime for the embedded phase based on Stage I identification with HCO$^+$ spatial mapping depends on how one treats the confused sources. If all confused sources are assumed to be Stage I, then the Perseus and Taurus sample together have 30% of Class 0+I sources misidentified. On the contrary, if all confused sources are assumed to be Stage II, then the sample would have 46% of sources misidentified. Using the updated Heiderman & Evans (2015) value as a reference, new estimates for the Stage I lifetime would then be 0.38 Myr and 0.29 Myr, respectively. It is more realistic to assume that confused sources are distributed between the two Stages, but correct classification using spatial mapping will still result in overall shorter timescales for Stage I objects.

5. LOMASS Database

Over the past decade, the molecular astrophysics group at the Leiden Observatory has observed a comprehensive dataset of

various molecular lines toward a large number of Class 0+I YSOs as part of various research projects. Such single-dish data provides a wealth of information which can be more easily exploited if collected together in a coherent way in one place. Therefore the *Single-dish Submillimeter Spectral Database of Low-mass YSOs hosted at Leiden Observatory* (LOMASS)[4] database has been established as a public web archive to fulfill this aim and provide a service to the community.

This database not only contains data from the observing projects conducted at the Leiden Observatory, but also molecular data on the same or other new sources which have been obtained from public data archives during the course of various projects. To date, observations from the JCMT and Atacama Pathfinder EXperiment (APEX, especially the CHAMP+ instrument) are included. Other relevant molecular spectral data of low mass YSOs from other telescopes, such as *Herschel*, the IRAM 30-m, etc. could be also included in the future.

Depending on availability, the database presents spectral maps and single pointing observations. Users can search via the web interface using one of two options - by source name or by molecular line name. In cases where the source names are not familiar, it is possible to generate a source list which provides source coordinates.

Once a source is selected, a page provides metadata about the source and available observations. Examples include the source coordinates, $V_{\rm lsr}$, telescope and instrument names, the beam efficiency that was used during data reduction and the rest frequency of the observations. Other source properties such as $L_{\rm bol}$, $T_{\rm bol}$, $M_{\rm env}$ and $n_{1000\rm AU}$ etc. are included, if available, with references to the papers these are drawn from. The "Downloads Corner" provides raw data in CLASS format, as well as reduced data in CLASS and/or FITS format.

In the case of single pointing observations, some of the observed quantities from the spectra are automatically extracted or calculated and then listed in each page. Examples include the observation date and rms noise of spectrum, together with the FWHM, integrated intensity and peak intensity of the specified molecular transition. The velocity range used in the integrated intensity calculation is also indicated.

For mapping observations, both integrated intensity and spectral maps are provided. In addition, the spectrum from the central region is included to aid quick comparison with other sources. The observed quantities for single pointing observations mentioned above are also given for map central spectra.

This database of single-dish spectral data for low-mass YSOs will provide a valuable and easily accessible reference for higher resolution interferometry data, especially the Atacama Large Millimeter/submillimeter Array (ALMA).

6. Conclusions

We have presented molecular line emission maps of HCO^+ 4–3 and $C^{18}O$ 3–2 observed with HARP on the JCMT, as well as SCUBA 450/850 μm and *Herschel* PACS 70/160 μm dust continuum maps to characterize the emission morphology of 56 candidate YSOs in the Perseus and Taurus clouds. An additional nine sources in Serpens observed in $C^{18}O$ 3–2 with HARP are also presented in this paper. The footprints of the $2'\times2'$ spatial maps enable qualitative categorization of the morphology and quantitative analysis of the concentration of emission from each source.

[4] http://lomass.strw.leidenuniv.nl

Four types of emission morphology are identified: on-source concentrated, offset concentrated, extended and non-detection. Calculation of the concentration factor for each source in HCO^+ 4–3 and 850 μm determines the stage classification where Stage I corresponds to embedded YSOs and Stage II corresponds to an evolved PMS star with a disk.

Conclusions of this work are:

- Previous methods of classifying the evolutionary stages of YSOs cannot always correctly identify Stage I sources in the embedded phase. Using the concentration factor of HCO^+ 4–3 as a way to identify truly embedded objects, we find that approximately 30% of Stage I sources in Perseus and Taurus are incorrectly classified. The 56 source sample between these two star forming regions consists of 32 truly embedded Stage I sources and 17 more evolved Stage II PMS stars with disks.
- The Perseus cloud hosts a higher percentage of Stage I sources compared to Taurus in our sample. Perseus has a population that is 71% (24 of 34 sources) embedded Stage I objects while Taurus consists of 68% (15 of 22 sources) more evolved Stage II objects.
- Nine sources in the sample cannot be identified as either Stage I or Stage II. Their emission in HCO^+ 4–3 may be strong or weak but their morphologies show a central peak that is offset from the source position by 20″ in most cases. Interferometric data is needed to further identify their nature.
- Using only the detection of HCO^+ at the source position as a criterion for identifying truly embedded sources is not as robust as classification with the spatial concentration. The single pointing method can result in up to 30% of sources being misidentified as embedded.
- Stage I lifetimes may be overpredicted on the order of 30%. The current timescale estimate for Stage I is 0.54 Myr. After correcting misidentified sources using HCO^+ spatial mapping the Stage I lifetime is 0.38 Myr, but may be as low as 0.29 Myr depending on how one treats the confused sources in this study.

The correct classification of YSOs in star forming regions such as Perseus and Taurus will lead to more complete sample of YSO evolutionary stages used to determine stage lifetimes. A comprehensive understanding of the stage of these YSOs will help future surveys selectively target embedded YSOs or evolved PMS stars with disks. Additional data with interferometers such as the Plateau de Bure Interferometer (PdBI), Submillimeter Array (SMA), and Atacama Large Millimeter/submillimeter Array (ALMA) will allow detailed investigation of the ongoing chemistry and kinematics of such objects.

Acknowledgements. The authors are grateful to Amanda Heiderman and Neal Evans for their useful collaboration and discussion on embedded protostellar environments. Many thanks to the referee, Charles Lada, for his very useful comments and suggestions. Astrochemistry in Leiden is supported by the Netherlands Research School for Astronomy (NOVA), by a Royal Netherlands Academy of Arts and Sciences (KNAW) professor prize, by a Spinoza grant and grant 614.001.008 from the Netherlands Organisation for Scientific Research (NWO). The authors are indebted to the various observers who have collected data for their papers and kindly provided them to be included in the LOMASS database, as well as staff at the JAC. Acknowledgment is given to the following programs and languages for building this database: GILDAS-CLASS and PYTHON for data reduction and format manipulation; PYTHON-MATPLOTLIB for plotting; MySQL for construction of the database; PHP and HTML for the web interface.

References

Adams, F. C., Lada, C. J., & Shu, F. H. 1987, ApJ, 312, 788

André, P., Men'shchikov, A., Bontemps, S., et al. 2010, A&A, 518, L102
Andre, P., Ward-Thompson, D., & Barsony, M. 2000, Protostars and Planets IV, 59
Beichman, C. A., Neugebauer, G., Habing, H. J., Clegg, P. E., & Chester, T. J., eds. 1988, Infrared astronomical satellite (IRAS) catalogs and atlases. Volume 1: Explanatory supplement, Vol. 1
Brandner, W., Sheppard, S., Zinnecker, H., et al. 2000, A&A, 364, L13
Brinch, C. & Jørgensen, J. K. 2013, A&A, 559, A82
Buckle, J. V., Hills, R. E., Smith, H., et al. 2009, MNRAS, 399, 1026
Casali, M. M. & Matthews, H. E. 1992, MNRAS, 258, 399
Connelley, M. S. & Greene, T. P. 2010, AJ, 140, 1214
Crapsi, A., van Dishoeck, E. F., Hogerheijde, M. R., Pontoppidan, K. M., & Dullemond, C. P. 2008, A&A, 486, 245
Dent, W., Duncan, W., Ellis, M., et al. 2000, in Astronomical Society of the Pacific Conference Series, Vol. 217, Imaging at Radio through Submillimeter Wavelengths, ed. J. G. Mangum & S. J. E. Radford, 33
Di Francesco, J., Johnstone, D., Kirk, H., MacKenzie, T., & Ledwosinska, E. 2008, ApJS, 175, 277
Doppmann, G. W., Greene, T. P., Covey, K. R., & Lada, C. J. 2005, AJ, 130, 1145
Dunham, M. M., Crapsi, A., Evans, II, N. J., et al. 2008, ApJS, 179, 249
Enoch, M. L., Glenn, J., Evans, II, N. J., et al. 2007, ApJ, 666, 982
Evans, II, N. J., Allen, L. E., Blake, G. A., et al. 2003, PASP, 115, 965
Evans, II, N. J., Dunham, M. M., Jørgensen, J. K., et al. 2009, ApJS, 181, 321
Fedele, D., Bruderer, S., van Dishoeck, E. F., et al. 2013, A&A, 559, A77
Greene, T. P. & Lada, C. J. 1996, AJ, 112, 2184
Gregersen, E. M., Evans, II, N. J., Zhou, S., & Choi, M. 1997, ApJ, 484, 256
Haisch, Jr., K. E., Lada, E. A., & Lada, C. J. 2001, ApJ, 553, L153
Hartmann, L. 2002, ApJ, 578, 914
Heiderman, A. & Evans, II, N. J. 2015, ApJ, 806, 231
Hogerheijde, M. R. & van der Tak, F. F. S. 2000, A&A, 362, 697
Hogerheijde, M. R., van Dishoeck, E. F., Blake, G. A., & van Langevelde, H. J. 1997, ApJ, 489, 293
Holland, W. S., Robson, E. I., Gear, W. K., et al. 1999, MNRAS, 303, 659
Johnstone, D., Fich, M., Mitchell, G. F., & Moriarty-Schieven, G. 2001, ApJ, 559, 307
Jørgensen, J. K., Johnstone, D., Kirk, H., & Myers, P. C. 2007, ApJ, 656, 293
Jørgensen, J. K., van Dishoeck, E. F., Visser, R., et al. 2009, A&A, 507, 861
Karska, A., Kristensen, L. E., van Dishoeck, E. F., et al. 2014, A&A, 572, A9
Kenyon, S. J. & Hartmann, L. 1987, ApJ, 323, 714
Kenyon, S. J. & Hartmann, L. 1995, ApJS, 101, 117
Kirk, H., Johnstone, D., & Di Francesco, J. 2006, ApJ, 646, 1009
Kristensen, L. E., van Dishoeck, E. F., Bergin, E. A., et al. 2012, A&A, 542, A8
Lada, C. J. & Wilking, B. A. 1984, ApJ, 287, 610
Lahuis, F., van Dishoeck, E. F., Boogert, A. C. A., et al. 2006, ApJ, 636, L145
Lommen, D., Jørgensen, J. K., van Dishoeck, E. F., & Crapsi, A. 2008, A&A, 481, 141
Mardones, D., Myers, P. C., Tafalla, M., et al. 1997, ApJ, 489, 719
Marseille, M. G., van der Tak, F. F. S., Herpin, F., & Jacq, T. 2010, A&A, 522, A40
Mottram, J. C., Hoare, M. G., Davies, B., et al. 2011, ApJ, 730, L33
Mottram, J. C., Kristensen, L. E., van Dishoeck, E. F., et al. 2014, A&A, 572, A21
Mottram, J. C., van Dishoeck, E. F., Schmalzl, M., et al. 2013, A&A, 558, A126
Muench, A. A., Lada, C. J., Luhman, K. L., Muzerolle, J., & Young, E. 2007, AJ, 134, 411
Myers, P. C., Evans, II, N. J., & Ohashi, N. 2000, Protostars and Planets IV, 217
Myers, P. C. & Ladd, E. F. 1993, ApJ, 413, L47
Poglitsch, A., Waelkens, C., Geis, N., et al. 2010, A&A, 518, L2
Riviere-Marichalar, P., Ménard, F., Thi, W. F., et al. 2012, A&A, 538, L3
Robitaille, T. P., Whitney, B. A., Indebetouw, R., Wood, K., & Denzmore, P. 2006, ApJS, 167, 256
Salyk, C., Herczeg, G. J., Brown, J. M., et al. 2013, ApJ, 769, 21
Shu, F. H. 1977, ApJ, 214, 488
Spezzi, L., Alcalá, J. M., Covino, E., et al. 2008, ApJ, 680, 1295
Tafalla, M., Myers, P. C., Mardones, D., & Bachiller, R. 2000, A&A, 359, 967
Tamura, M., Gatley, I., Waller, W., & Werner, M. W. 1991, ApJ, 374, L25
Thi, W.-F., van Zadelhoff, G.-J., & van Dishoeck, E. F. 2004, A&A, 425, 955
van Kempen, T. A., van Dishoeck, E. F., Salter, D. M., et al. 2009, A&A, 498, 167
Vorobyov, E. I. & Basu, S. 2015, ApJ, 805, 115
Walawender, J., Bally, J., Kirk, H., & Johnstone, D. 2005, AJ, 130, 1795
Walker-Smith, S. L., Richer, J. S., Buckle, J. V., Hatchell, J., & Drabek-Maunder, E. 2014, MNRAS, 440, 3568
White, R. J. & Hillenbrand, L. A. 2004, ApJ, 616, 998
Whitney, B. A., Wood, K., Bjorkman, J. E., & Cohen, M. 2003a, ApJ, 598, 1079
Whitney, B. A., Wood, K., Bjorkman, J. E., & Wolff, M. J. 2003b, ApJ, 591, 1049
Williams, J. P., de Geus, E. J., & Blitz, L. 1994, ApJ, 428, 693

Appendix A: Notes on Individual Sources

J032536.4+304523 (L1448-N): Note that the $C^{18}O$ 3–2 map is incomplete, with bad pixels flagged in a rectangular region from (0″, 0″) to (40″, -50″). The flagged data is not immediately apparent in the spatial maps due to interpolation, but it is easily seen in the spectral map. (See entry in the LOMASS database.)

J032738.2+301358 (L1455-FIR 2): Another sub-mm object, L1455-IRS 1, lies at offset (20″, -60″) and dominates emission in the map. Concentrated HCO^+ 4–3 emission from the source is still apparent in the spatial map.

J032743.2+301228 (L1455-IRS 4): Another sub-mm object, L1455-IRS 1, lies at offset (-60″, 40″) and dominates emission in the map. There is widespread emission of HCO^+ 4–3 seen in the spectral map from the northwest corner to the southeast corner. However, concentrated HCO^+ 4–3 emission from the source is still apparent above this strong background.

J032834.5+310705: The source has a high 850 μm concentration, but cannot be properly analyzed due to contaminating absorption features in the molecular line maps.

J032859.5+312146: HCO^+ 4–3 spectral map indicates a slight broadening of the line off-source, there appear to be no other nearby YSOs or dense cores that might contaminate the field.

J032900.6+311200: HCO^+ 4–3 spectral map indicates a slight broadening of the line off-source, there appear to be no other nearby YSOs or dense cores that might contaminate the field.

J032901.6+312028: HCO^+ 4–3 spectral map indicates a slight broadening of the line off-source. The field of view contains three YSO or dense core objects, JCMTSF J032901.3+312031, SSTc2d J032901.6+312021, and [RAC97] VLA 43 that lie at an offset of about 8″ to the southwest.

J032903.3+311555: HCO^+ 4–3 spectral map indicates a slight broadening of the line off-source. The field contains Herbig Haro objects to the southeast and southwest, and a YSO (2MASS J03290289+3116010) at an offset of (-10″, -5″) that may contribute to the extended HCO^+ 4–3 emission.

J032904.0+311446 (HH 7-11 MMS6): shows strong, extended HCO^+ 4–3 throughout the field of view indicating the presence of large scale high density material that could host an embedded protostar, but the lack of a clear peak at the source position prevents definite Stage I classification. The J032904.0+311446 (HH 7-11 MMS6) spectral map does show evidence of line wings, suggesting that the extent of the emission may be due to outflows from the source or nearby objects.

J034350.9+320324: The map shows off-source emission in HCO^+ 4–3 due to a binary companion at offset (0,+15″).

J032910.7+311820: The map shows off-source emission in HCO^+ 4–3 due to a binary companion at offset (+10″,+10″).

J032951.8+313905: HCO^+ 4–3 spectral map indicates a slight broadening of the line off-source, there appear to be no other nearby YSOs or dense cores that might contaminate the field.

J033313.8+312005: The source has a high concentration in HCO^+ 4–3, but weak integrated intensity just at the threshold for consideration as a Stage I object. It has a low concentration in SCUBA 850 μm emission, and the $C^{18}O$ 3–2 map contained emission and absorption in the line profiles, preventing proper characterization. The source is marked as confused due to the $C^{18}O$ 3–2 contamination, but other tracers are more consistent with Stage II properties.

J033314.4+310710 (B1-SMM3): A weak outflow wing can be seen in the HCO^+ 4–3 central spectrum. Two objects – SSTc2d J033316.7+310755 and B1-IRS – lie at an offset of about (+50″, +40″), thus it is likely that the extended emission found in this map and line wings in the spectral profile are due to emission and outflows from these other objects in the field of view.

J033320.3+310721 (B1-b): A weak outflow wing can be seen in the HCO^+ 4–3 central spectrum. The map shows extended emission with a weak peak offset by about 15″. A much stronger peak at an offset of about (-50″, +30″) is due to emission from SSTc2d J033316.7+310755 and B1-IRS. No peaks in emission are located at the source position. In addition, the 850 μm emission has a low concentration factor, thus the object remains confused.

J034359.4+320035: The HCO^+ 4–3 map has emission peaking significantly off-source as a result of another object at an offset of about (-20″, +10″) as seen in all bands of molecular line and dust continuum emission. The source is categorized in nearly all maps as offset (O_{H7148} E_C). The nearby object SSTc2d J034357.6+320045 (Pers-45 from Jørgensen et al. 2007) is found at these coordinates. HCO^+ 4–3 is detected at the target source position, as seen in the central spectrum, but its spectral map shows that this emission cannot be disentangled from the secondary object. Contamination prevents calculation of the concentration factor in 850 μm and HCO^+ 4–3.

J034402.4+320204: The field of view contains HCO^+ 4–3 that is extended on scales of 40″ offsets. Though there is a peak within this extended emission, it has a low concentration factor that prevents a definite Stage I classification.

J042110.0+270142: The map shows off-source emission in HCO^+ 4–3 due to a binary companion at offset (-15″,+25″). Emission from J042111.4+270108 is seen at an offset of about (40″,-30″).

J042111.4+270108: The map shows extended HCO^+ 4–3 throughout the field due to a third object – J042110.0+270142 – at offset (-25″,+40″). There is an off-source peak at the location of the binary companion at offset (-25″,+25″). With no complementary SCUBA dust emission it cannot be properly classified.

Appendix B: Central Spectra

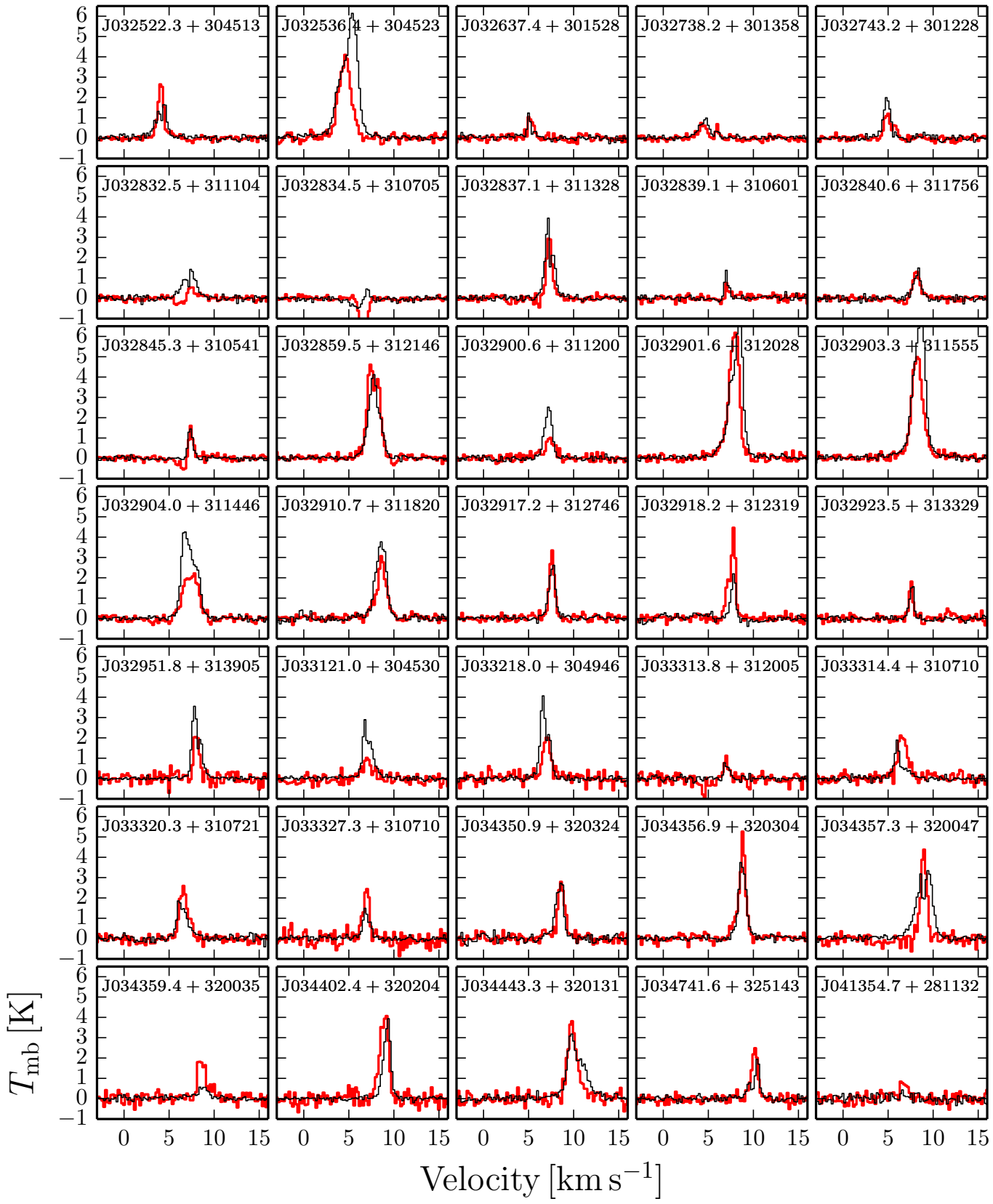

Fig. B.1: Central spectra for HCO^+ 4–3 (black) and $C^{18}O$ 3–2 (red) in a 15″ beam extracted from the source locations listed in Table 1.

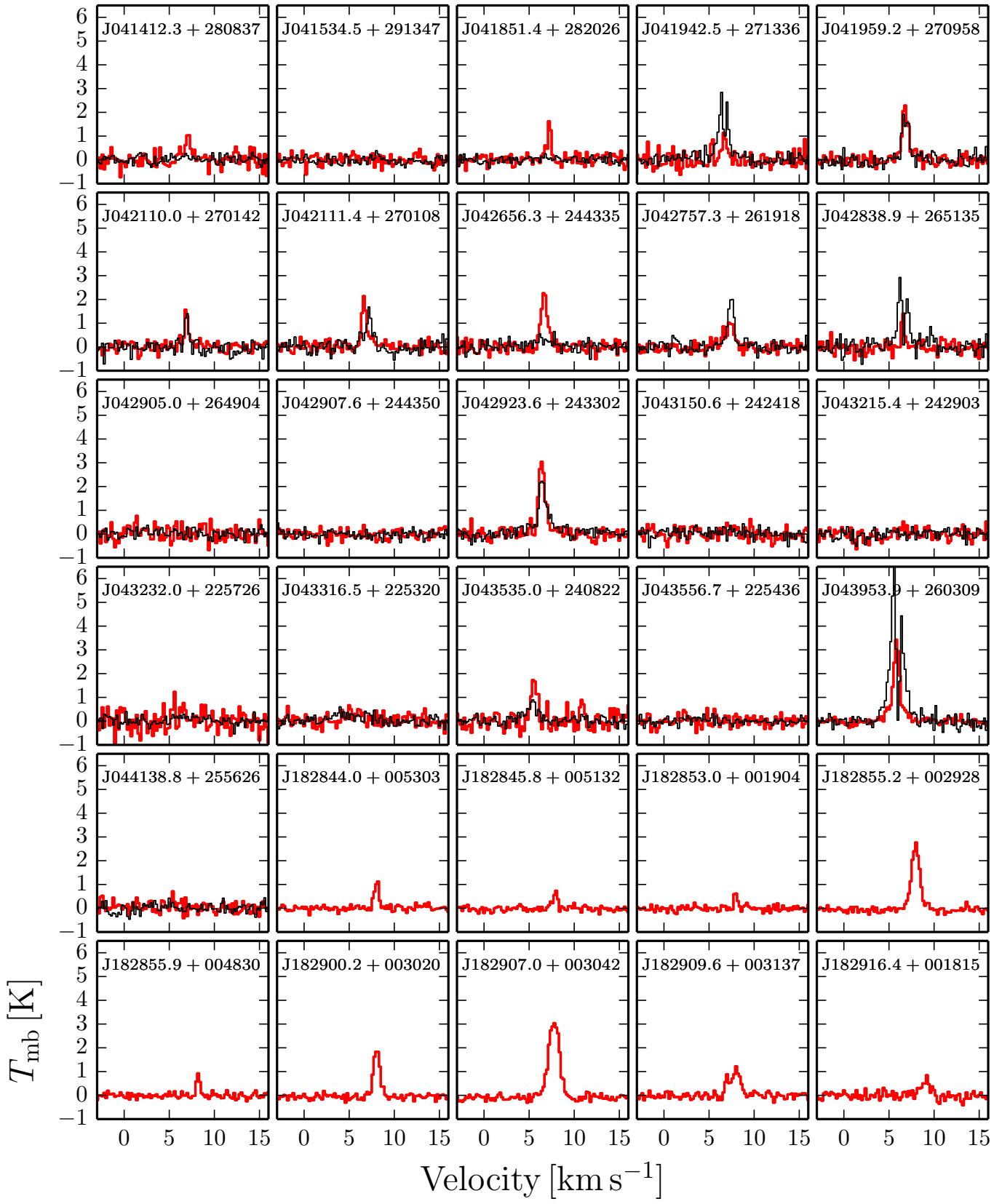

Fig. B.2: Central spectra for HCO^+ 4–3 (black) and $C^{18}O$ 3–2 (red) in a 15″ beam extracted from the source locations listed in Table 1.

Appendix C: Emission Maps

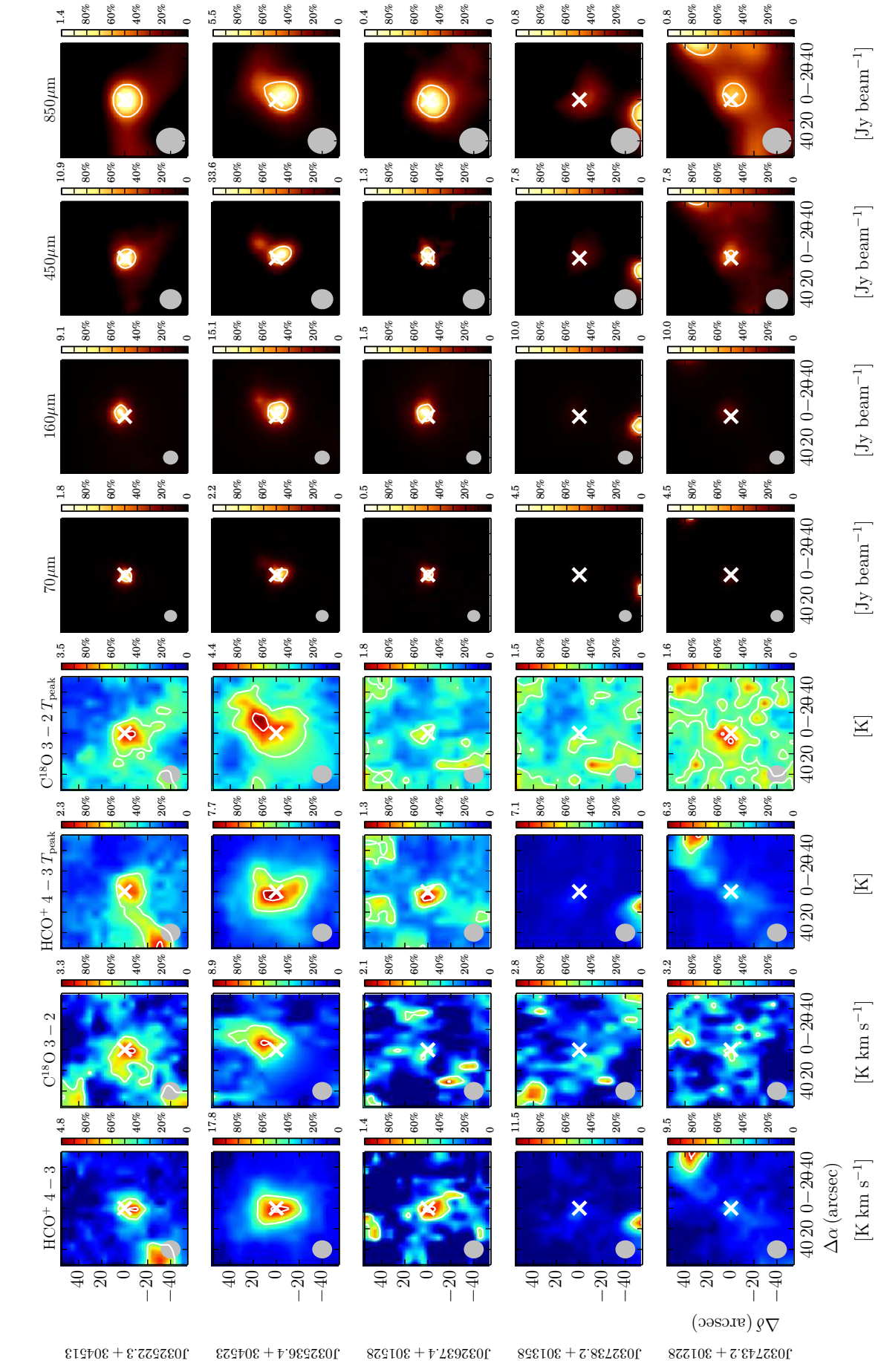

Fig. C.1: Perseus sources. $2' \times 2'$ maps of JCMT HARP HCO^+ 4–3 and $C^{18}O$ 3–2, *Herschel* PACS 70μm and 160μm continuum, and JCMT SCUBA 450μm and 850μm continuum. Each map has solid white contours at 50% and 90% of the peak emission. Color scaling is normalized to peak emission and shown as percentage values. Source location based on Table 1 is indicated by a white cross at the center of each image. There are two molecular line maps. The first shows the spectrally integrated intensity over the region. The second shows the peak temperature over the region. Filled gray circles in the lower left give the relevant beam sizes.

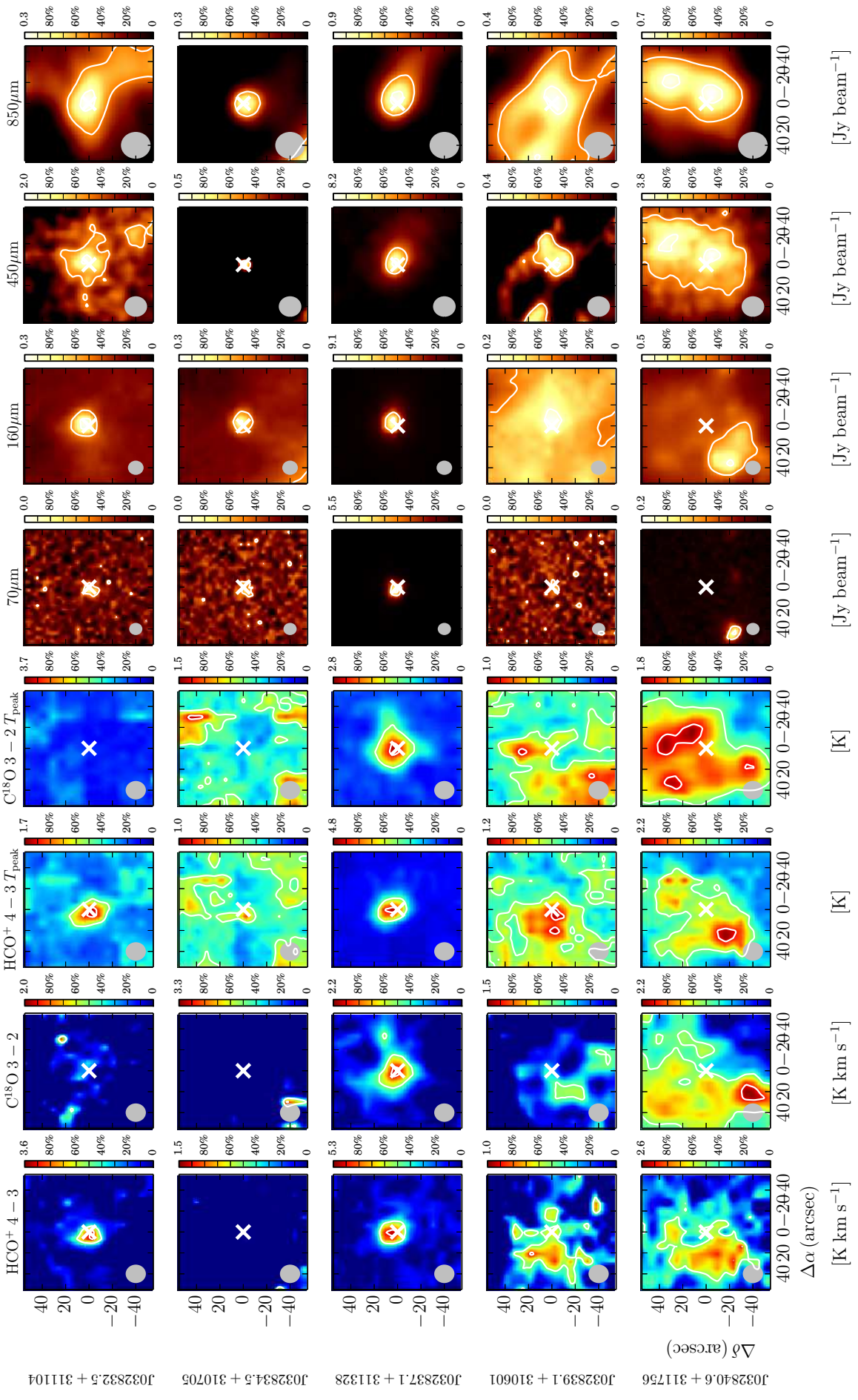

Fig. C.2: Perseus sources. See Figure C.1 for caption.

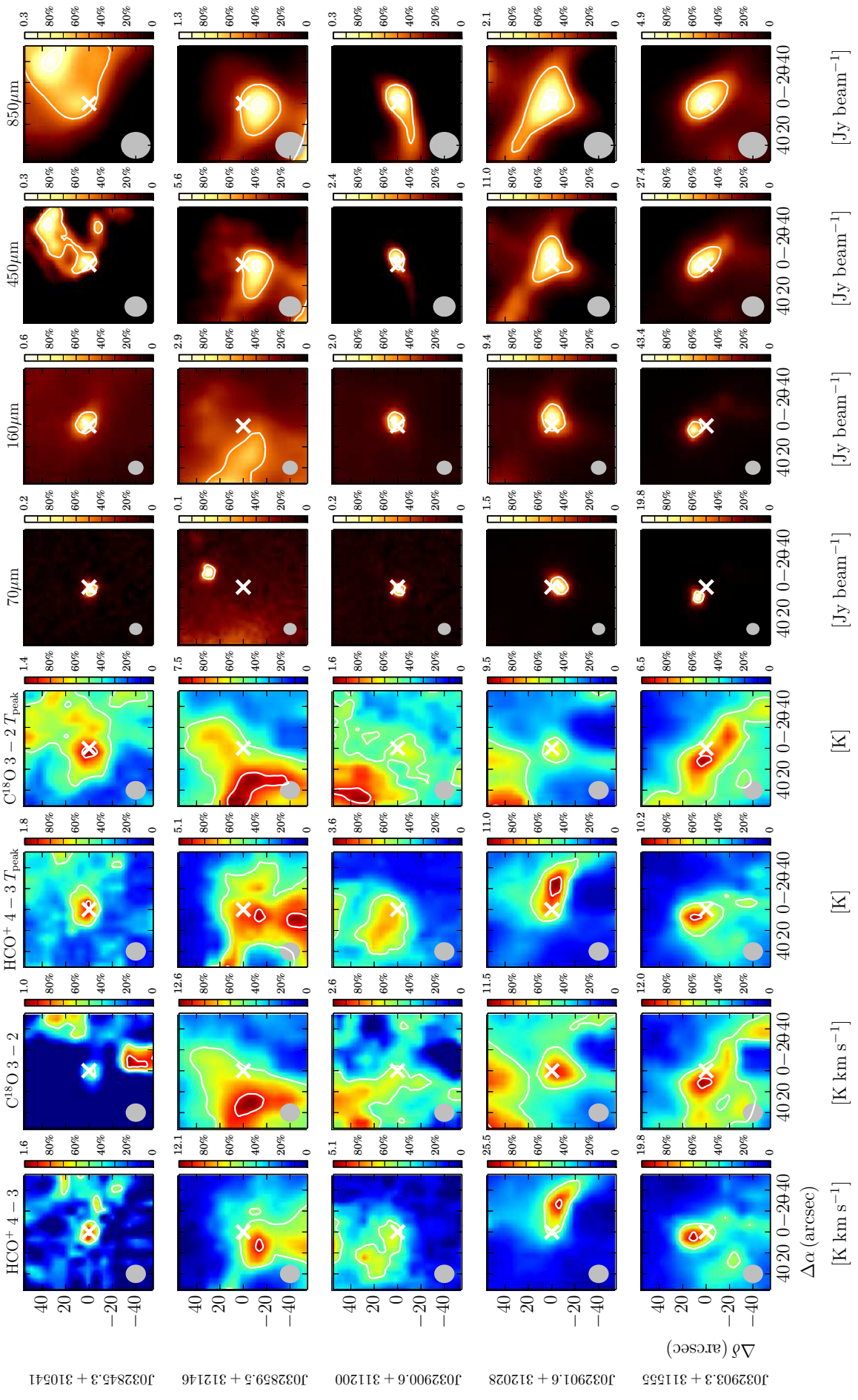

Fig. C.3: Perseus sources. See Figure C.1 for caption.

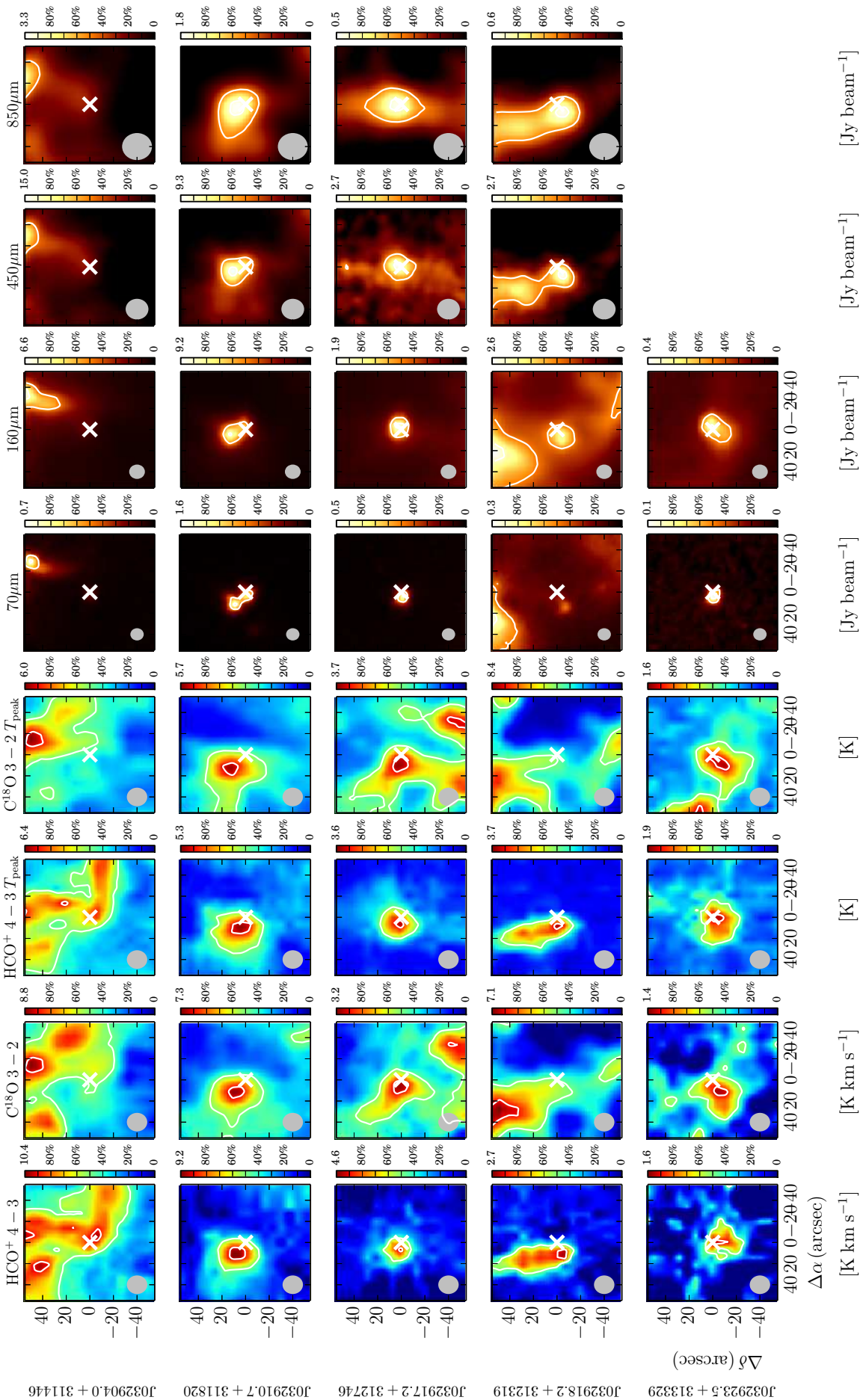

Fig. C.4: Perseus sources. See Figure C.1 for caption.

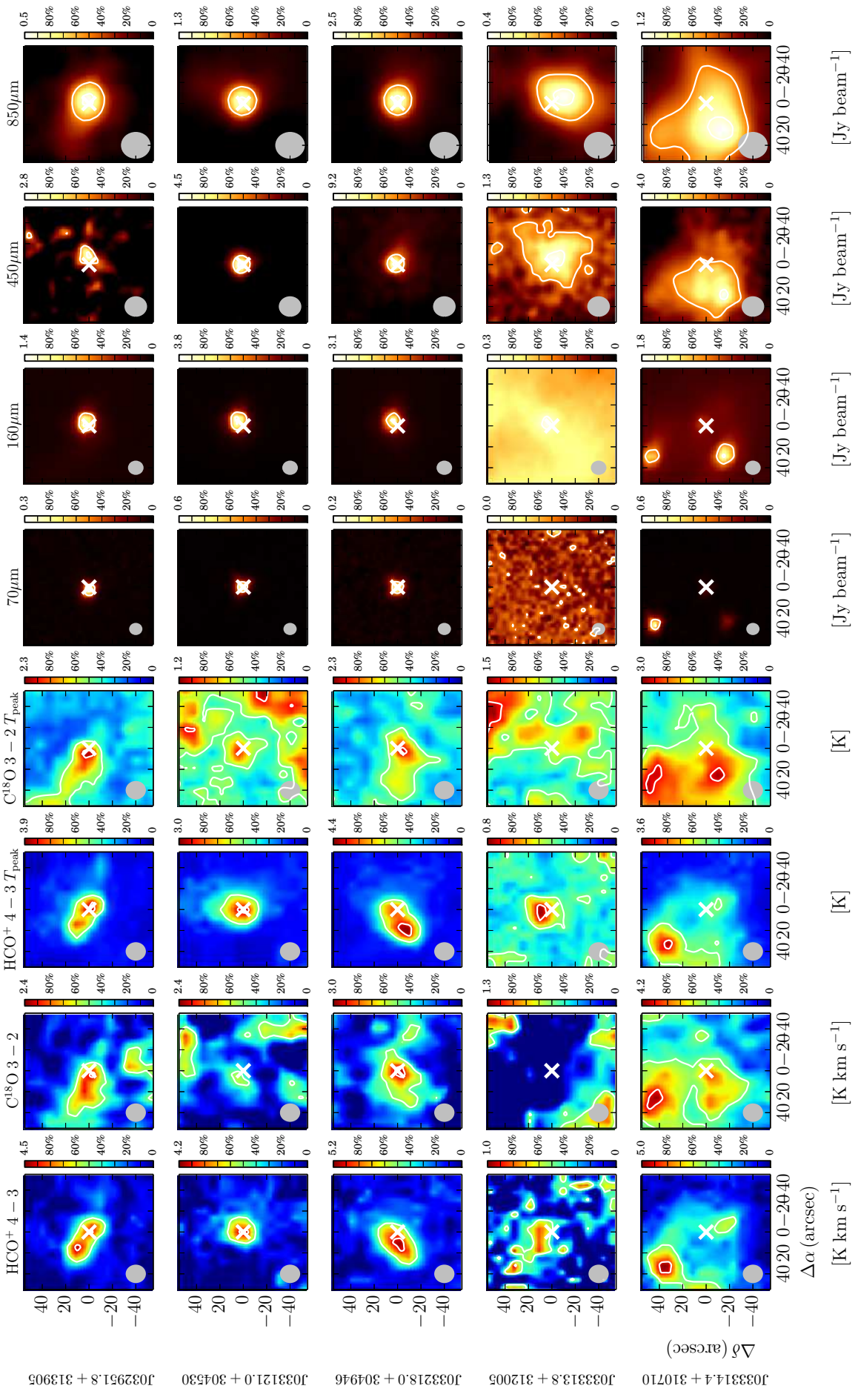

Fig. C.5: Perseus sources. See Figure C.1 for caption.

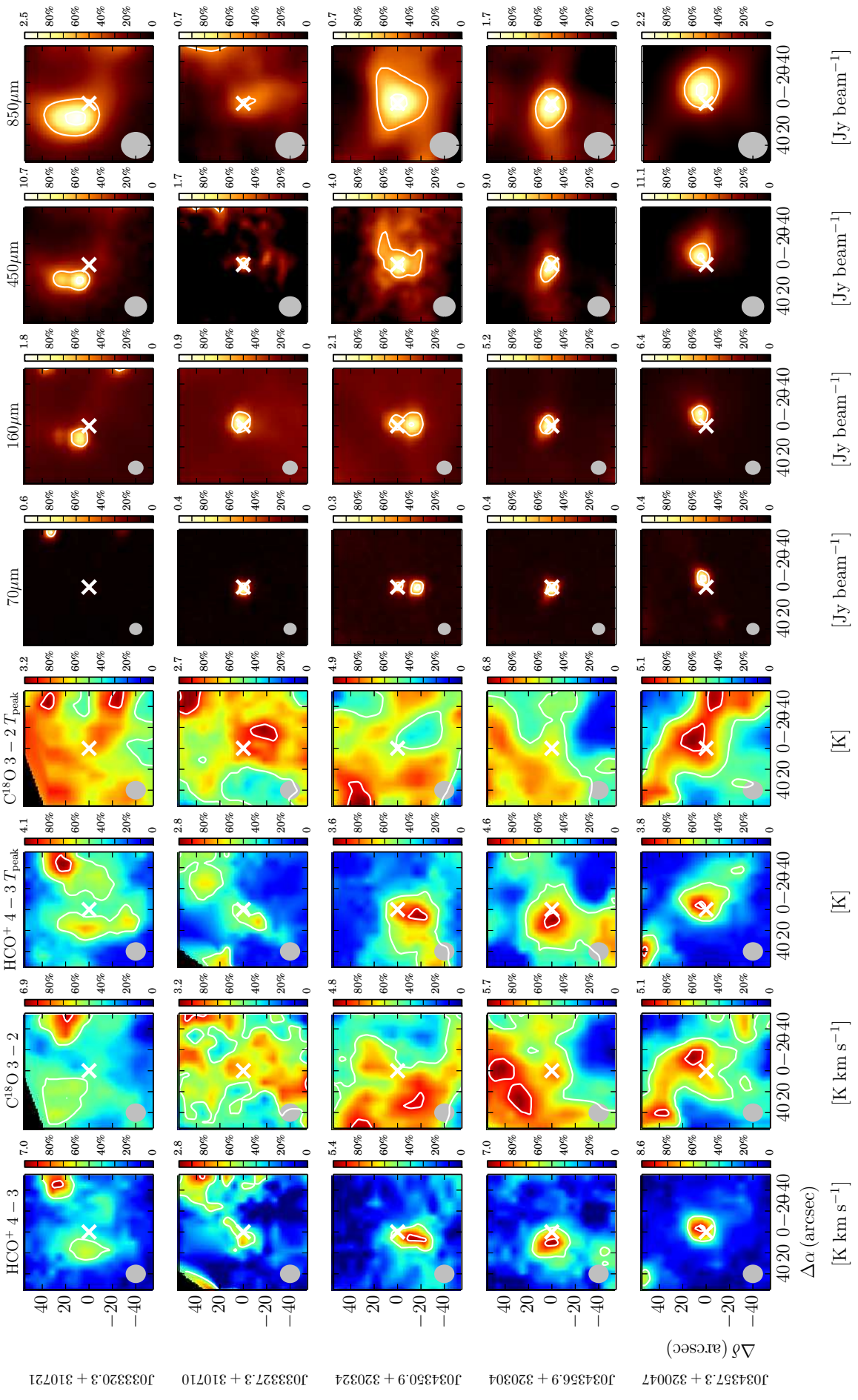

Fig. C.6: Perseus sources. See Figure C.1 for caption.

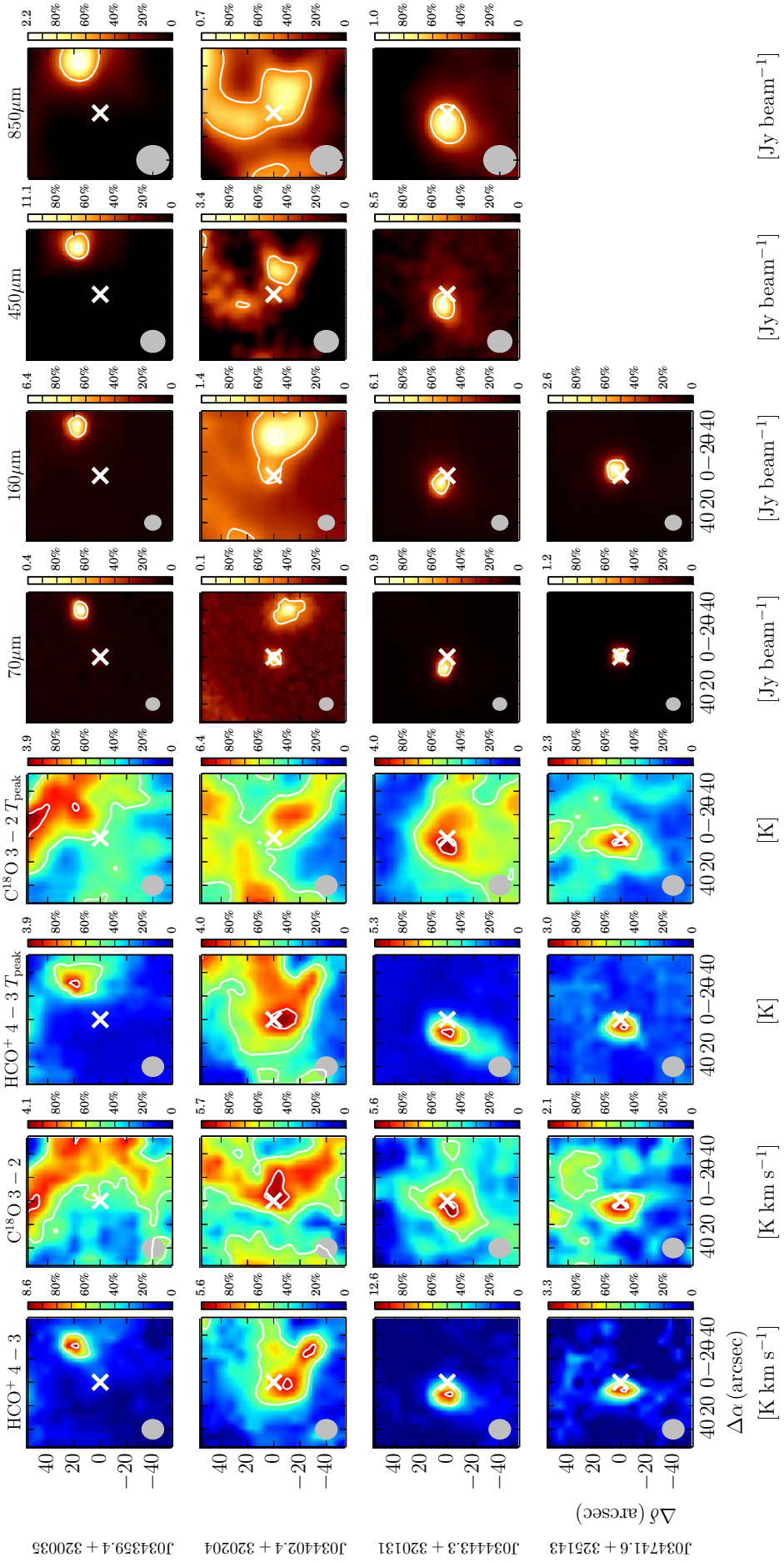

Fig. C.7: Perseus sources. See Figure C.1 for caption.

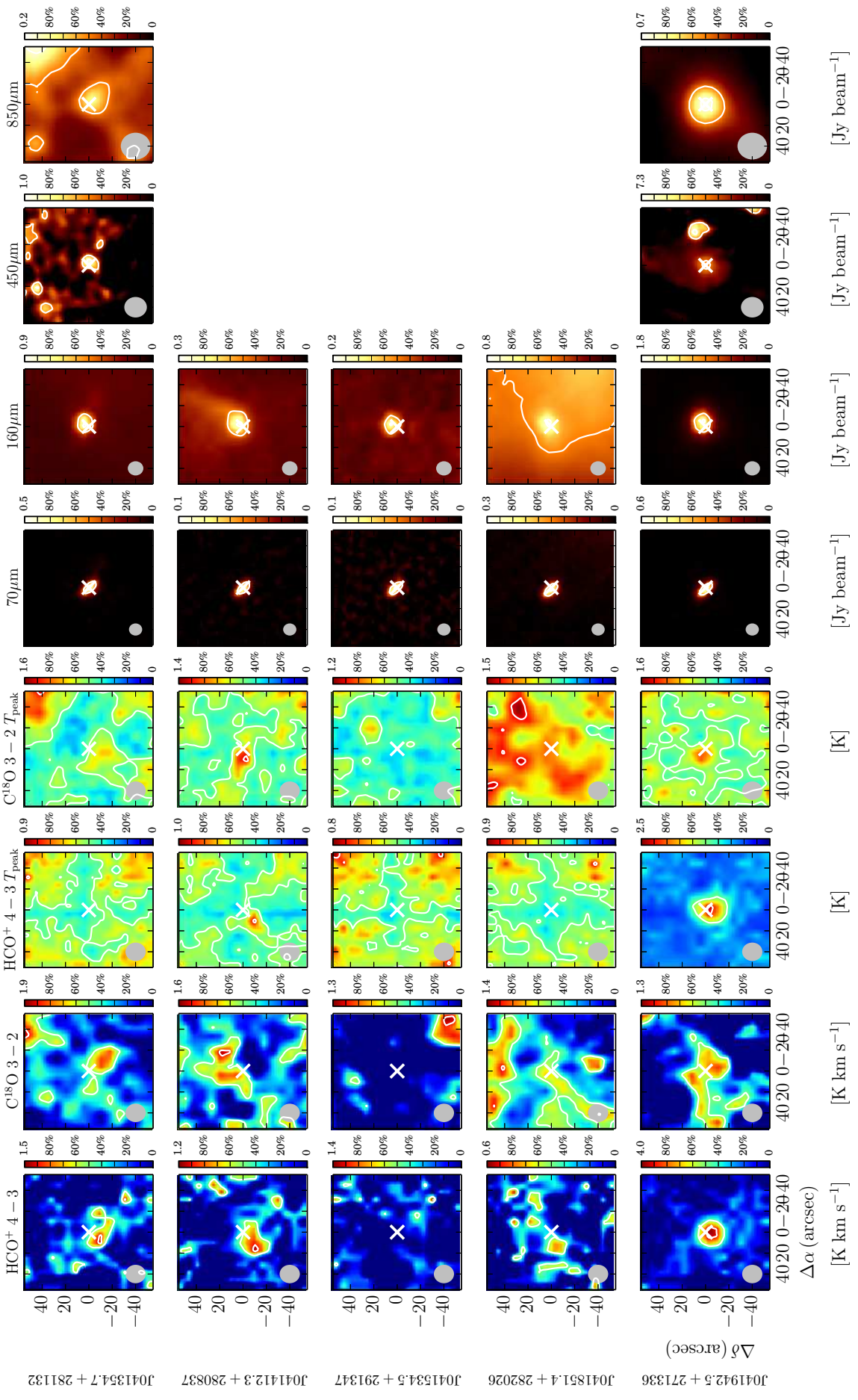

Fig. C.8: Taurus sources. See Figure C.1 for caption.

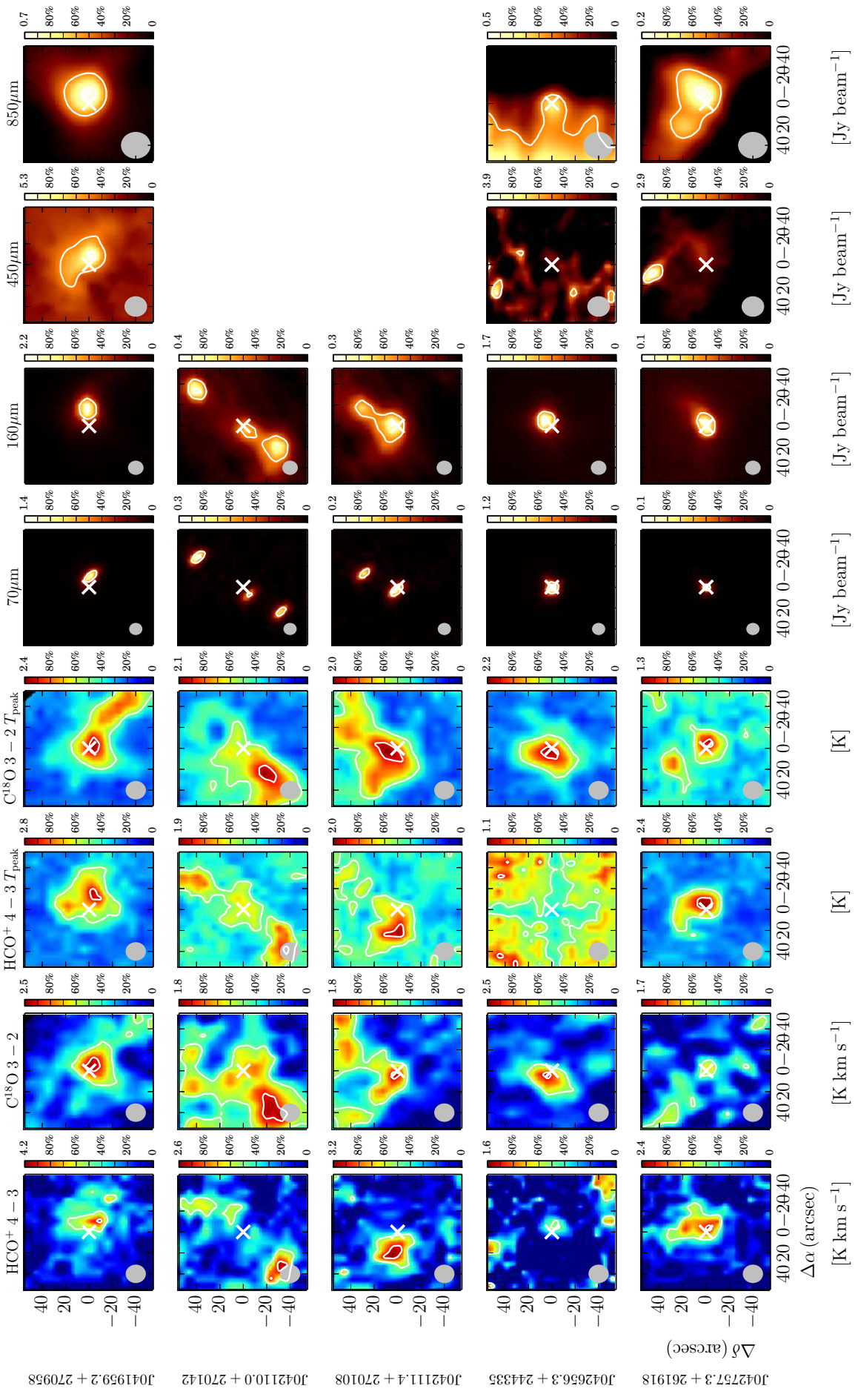

Fig. C.9: Taurus sources. See Figure C.1 for caption.

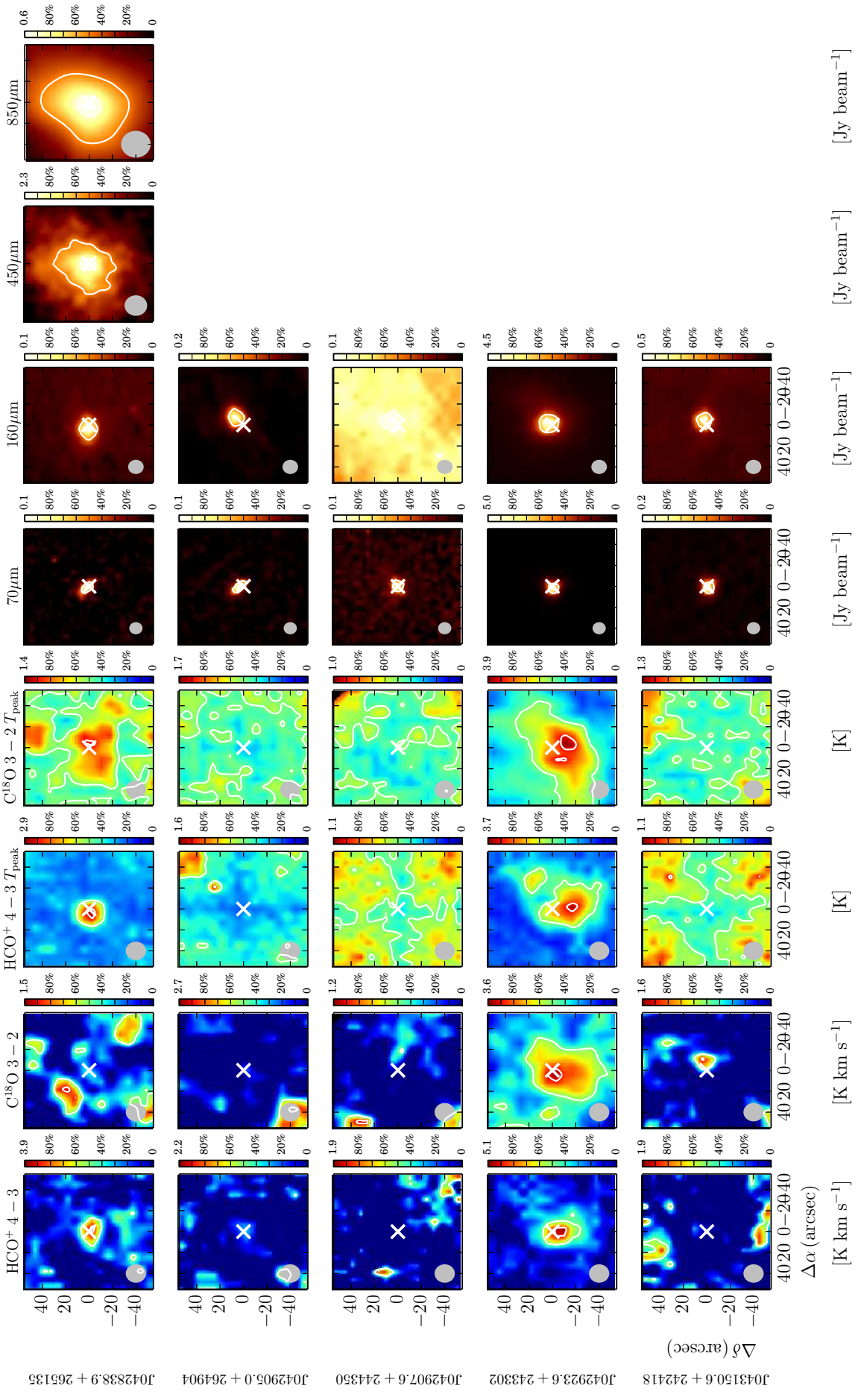

Fig. C.10: Taurus sources. See Figure C.1 for caption.

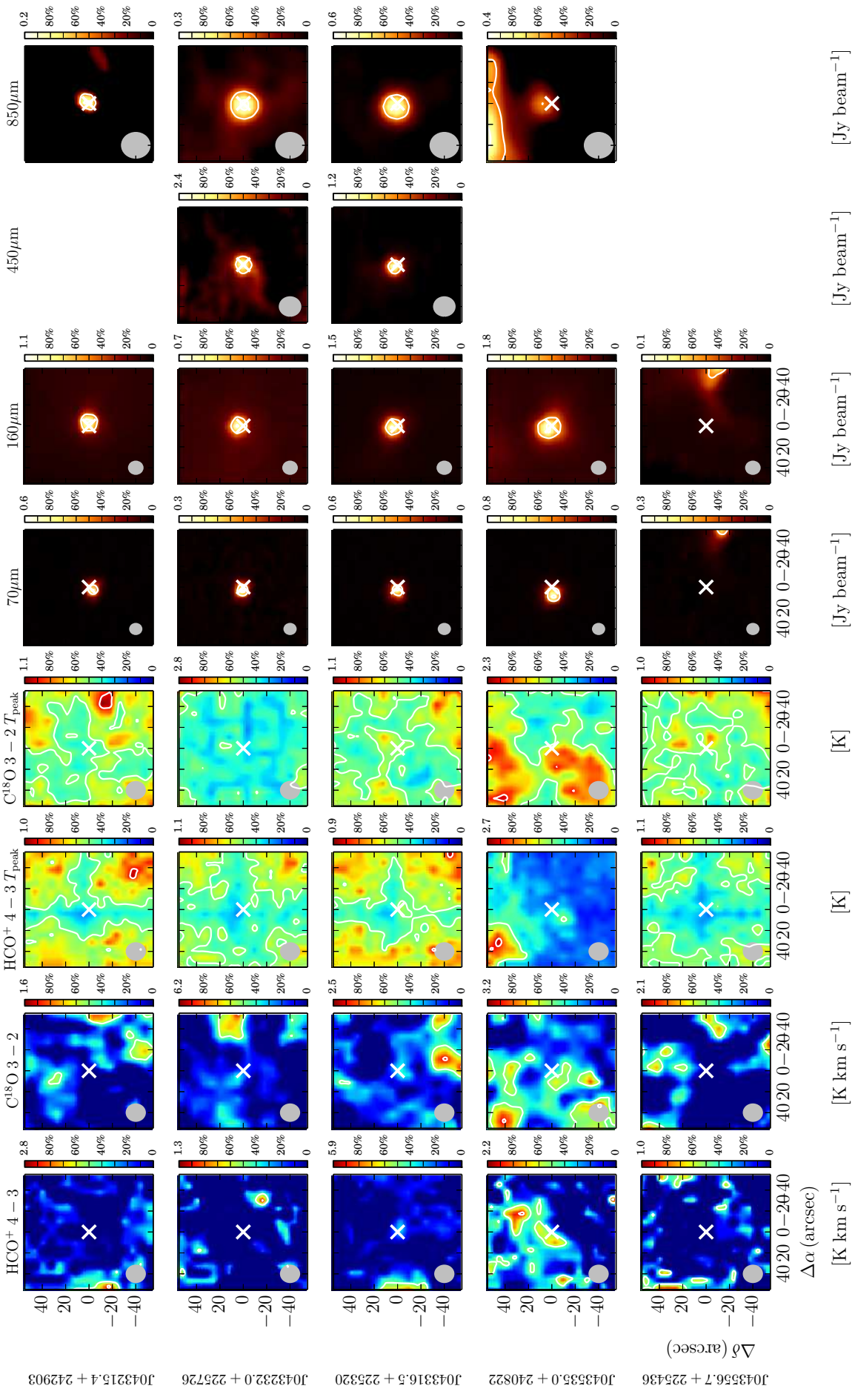

Fig. C.11: Taurus sources. See Figure C.1 for caption.

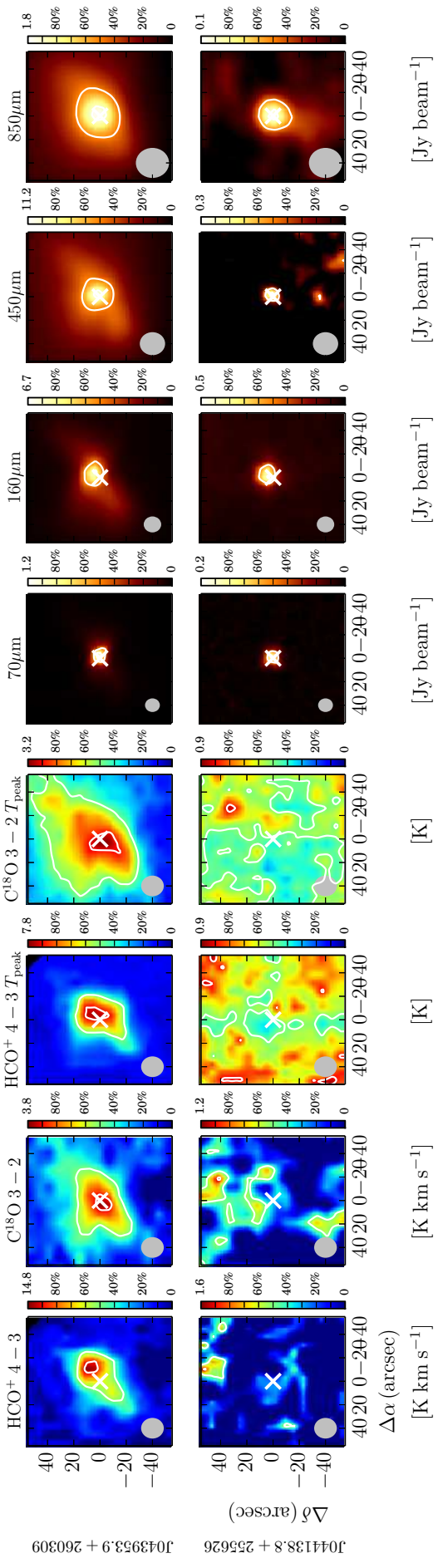

Fig. C.12: Taurus sources. See Figure C.1 for caption.

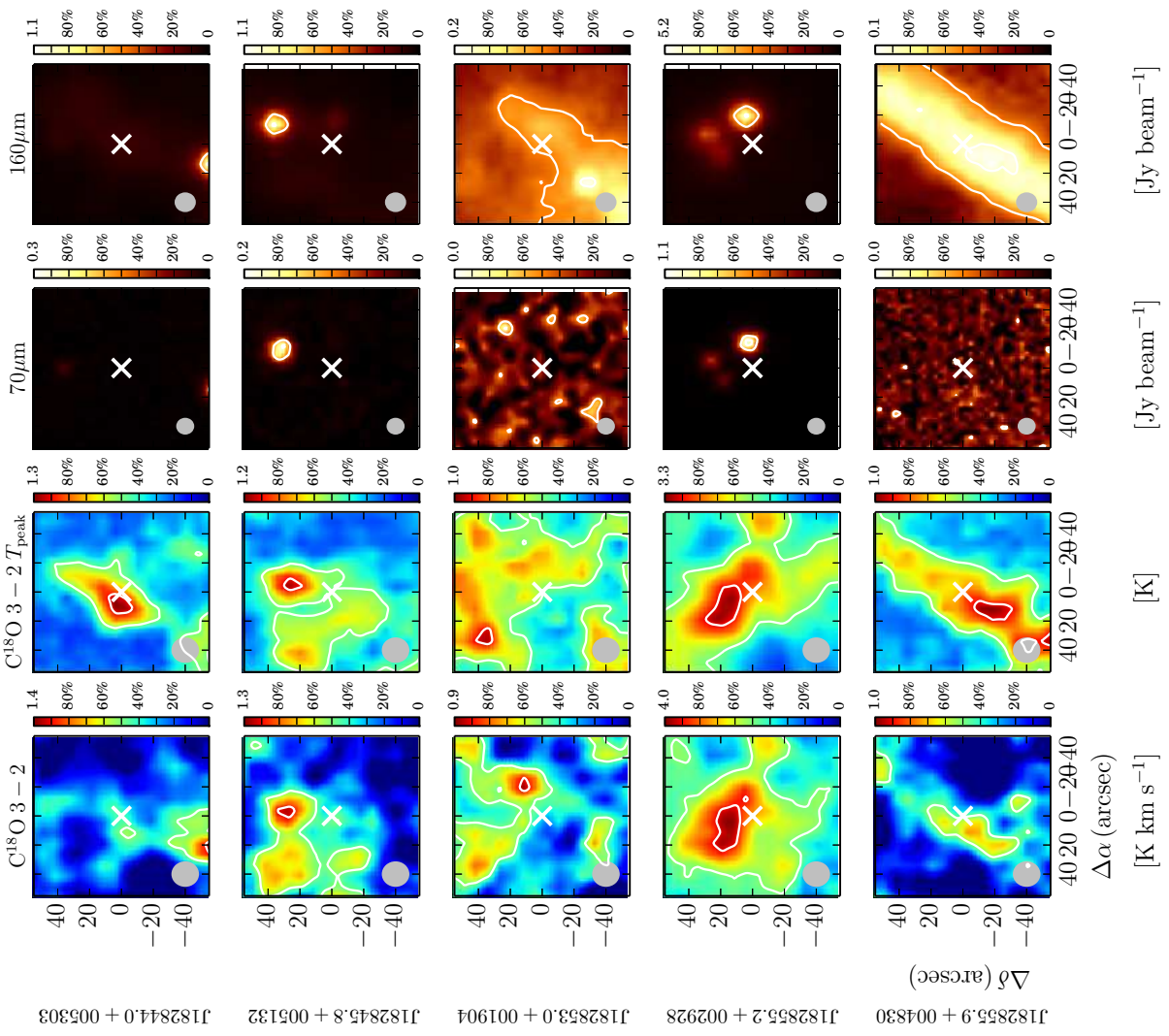

Fig. C.13: Serpens sources. See Figure C.1 for caption.

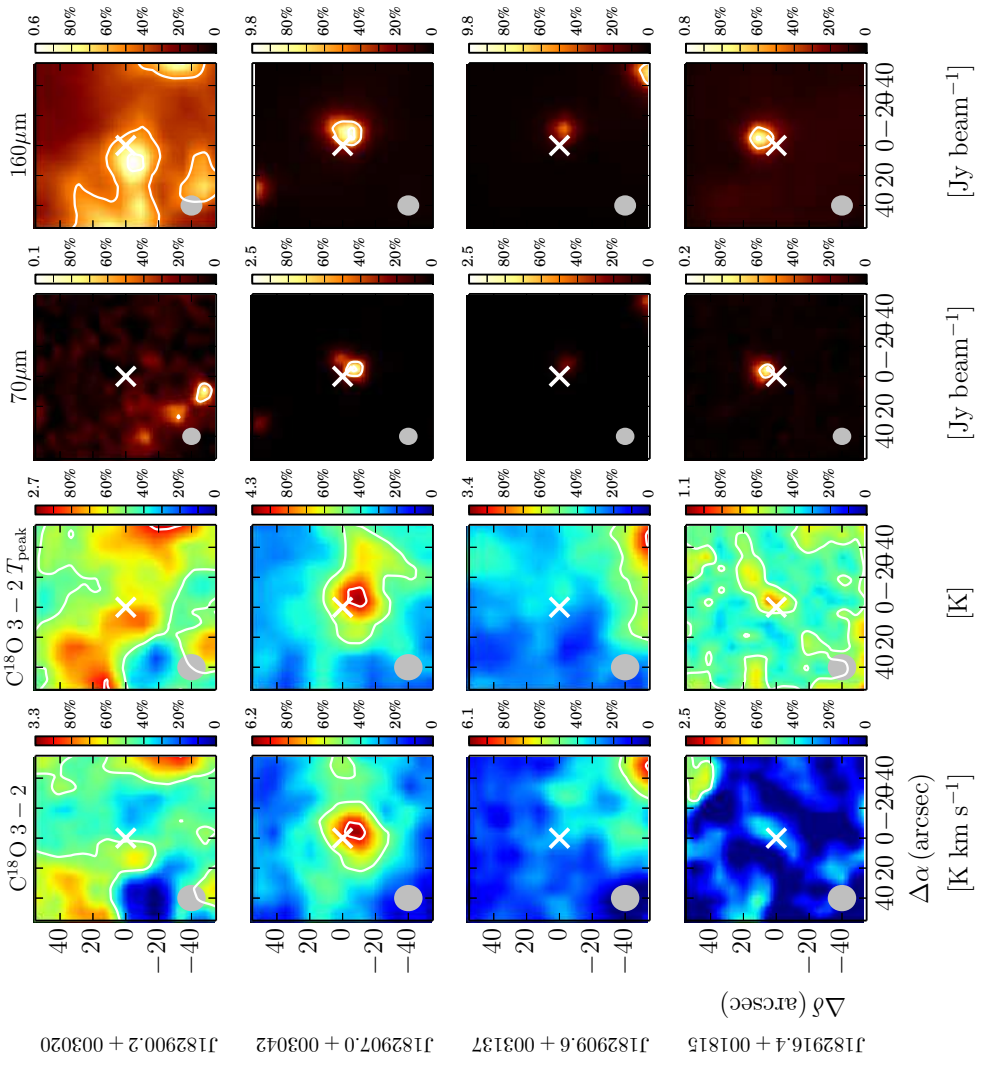

Fig. C.14: Serpens sources. See Figure C.1 for caption.